The chemical and Sm–Nd isotopic behaviour of accessory minerals in metasediments along the LP-HT Chugach Metamorphic Complex (Alaska)

Théo Biget, Emilie Bruand, Inês Pereira, Maud Boyet, Deta Gasser, Kurt Stüwe, Antonio Langone

Contributions to Mineralogy and Petrology (2024) 179:108
https://doi.org/10.1007/s00410-024-02185-2

ORIGINAL PAPER

The chemical and Sm–Nd isotopic behaviour of accessory minerals in metasediments along the LP-HT Chugach Metamorphic Complex (Alaska)

Théo Biget[1,2] · Emilie Bruand[2] · Inês Pereira[3] · Maud Boyet[1] · Deta Gasser[4] · Kurt Stüwe[5] · Antonio Langone[6]

Received: 4 July 2024 / Accepted: 11 November 2024 / Published online: 28 November 2024

Abstract

The study of accessory phases, including trace element concentrations and radiogenic isotopes, provides powerful information for a better understanding of geological processes such as crustal anatexis. These accessory minerals are the primary carriers of many incompatible elements and Rare Earth Elements (REE) in crustal rocks. In this contribution, we provide a detailed study on the chemical and isotopic (Nd isotopes) behaviour of accessory minerals within the Chugach Metamorphic Complex in Alaska. This Eocene (55−50 Ma) metamorphic complex developed in a Late Cretaceous to Paleogene accretionary prism consisting of metapelitic and metagreywacke rocks. The complex exposes a systematic N-S metamorphic gradient from greenschist to upper amphibolite facies (500 to ~ 700 °C) with anatexis under water-saturated conditions and minor muscovite breakdown. Trace element concentration data for apatite, monazite and titanite reveal a strong influence of bulk composition (greywacke vs. pelite) on their REE signatures in the migmatitic gneisses. In xenotime-bearing metapelitic samples, we show that monazite and apatite, which crystallised close to peak metamorphism, have their HREE-Y contents increasing with temperature within a narrow range of ~150 °C (550 to ~700 °C). While the influence of temperature on the Y content of monazite was already demonstrated before, we prove that apatite follow the same chemical behaviour. In these samples, partial melting process can be tracked via Eu/Eu* which decreases systematically from schist to migmatitic gneisses and is interpreted to be related to plagioclase crystallisation. Among all analysed samples (schists and migmatites), we observe no significant differences in εNd between monazite, allanite and whole-rock, regardless of rock type. This suggests (i) a general homogeneity of Nd isotopic composition above 550 °C up to crustal anatexis, and (ii) an isotopic equilibrium between mineral and whole-rock, indicating Nd isotopic disequilibria induced by partial melting are unlikely in this case study.

Keywords Crustal anatexis · In-situ Nd isotopes · REE-bearing minerals · Trace elements · LA-(MC)-ICP-MS · Metamorphic gradient

Communicated by Daniela Rubatto.

✉ Théo Biget
theo.biget@uca.fr

[1] Laboratoire Magmas et Volcans, Université Clermont Auvergne, Clermont-Ferrand, France

[2] Laboratoire Geo-Ocean, Université de Bretagne Occidentale, Brest, France

[3] Departamento de Ciências da Terra, Centro de Geociências, Universidade de Coimbra, Coimbra, Portugal

[4] Western Norway University of Applied Sciences, Bergen, Norway

[5] Institute of Earth Sciences, Karl-Franzens Universität, Graz, Austria

[6] Department of Earth and Environmental Sciences, University of Pavia, Pavia, Italy

Introduction

Apatite ($Ca_5(PO_4)_3(OH, F,Cl)$), monazite ($(LREE, Th)PO_4$), allanite ($(LREE, Ca, Y)_2(Al, Fe^{3+})_3(SiO_4)(OH)$), titanite ($CaTiSiO_5$), xenotime ($YPO_4$), and zircon ($ZrSiO_4$) are the main Rare Earth Element (REE) carriers in igneous and metamorphic rocks (e.g. Engi 2017; Volante et al. 2023) and constitute powerful tools for tracing geological processes such as partial melting and ultimately crustal differentiation (e.g. Brown and Rushmer 2006; Sawyer et al. 2011). Trace element analyses and phase equilibria modeling in pelitic and greywacke systems (e.g. Spear and Pyle 2010; Yakymchuk and Brown 2014; Shrestha et al. 2019; Johnson et al. 2021) have greatly improved our understanding of monazite (e.g. Skrzypek et al. 2018; Williams et al. 2022) and zircon stabilities (e.g. Kohn and Kelly 2018; Kunz et al. 2018) and their chemical behaviour during high temperature metamorphism and anatexis. These two phases can be used as geothermometers (e.g. Volante et al. 2023) and their trace elements can record metamorphic reactions involving other accessory minerals or major minerals such as garnet or plagioclase, allowing to reconstruct the *P-T* path history (e.g. Rubatto et al. 2013; Shrestha et al. 2019). Other studies have confirmed that bulk composition of sedimentary protoliths have an influence on the dissolution of zircon and monazite during anatexis. In particular, zircon and monazite are modelled to be stable at higher temperatures in a greywacke compared to a metapelite due to the lower fertility of the greywacke (Yakymchuk et al. 2017; Johnson et al. 2021). The chemical behaviour of some other ubiquitous accessory minerals like apatite during HT metamorphism and partial melting reactions (i.e. water-saturated melting, muscovite, biotite or amphibole breakdown reactions) is less understood with only few studies available (Bea and Montero 1999; Hammerli et al. 2014; Henrichs et al. 2019; O'Sullivan et al. 2020). In addition, most studies often focused on one single accessory phase while only few combine a multi-minerals approach along a metamorphic gradient reaching anatexis, dealing with various bulk-rock compositions and *P-T* conditions (e.g. Bingen et al. 1996; Bea and Montero 1999; Rubatto et al. 2006; Hansen and Harlov 2007; Hammerli et al. 2016; Shrestha et al. 2019). Therefore, establishing a comprehensive overview of the parameters (e.g. changing effective whole-rock composition, co-crystallisation of other accessory minerals, evolving *P-T* conditions and partial melting reactions) affecting the stability and the chemical signatures of accessory minerals during prograde metamorphism up to anatexis is challenging with the current available data from the literature.

Over the past 15 years, in situ Sm–Nd isotopes have been successfully measured in accessory phases that dominate the whole-rock (WR) Sm–Nd budget (i.e. monazite, allanite and to lesser extent apatite, titanite and xenotime), enhanced by recent analytical advances (e.g. Fisher et al. 2011, 2020a; Iizuka et al. 2011; Doucelance et al. 2020). These studies showed that these minerals can be used to obtain crystallisation ages (e.g. Hammerli et al. 2014, 2019; Hammerli and Kemp 2021) or determine the primary isotopic signatures of magma sources (e.g. Gregory et al. 2009; Iizuka et al. 2011; Fisher et al. 2017; Sun et al. 2021; Bruand et al. 2023). However, the existence of isotopic disequilibria during partial melting remains heavily debated in the literature (see review in Hammerli and Kemp 2021). The temperature at which the Sm–Nd isotopic system homogenises in different accessory phases during metamorphism is also not well constrained (Hammerli et al. 2014; Spandler et al. 2018; Hammerli and Kemp 2021). This uncertainty ultimately hampers our ability to confidently interpret isotopic signatures of accessory phases in rocks that have undergone complex geological histories, with multiple tectonic and thermal events, such as those found in Archaean terranes (Hammerli et al. 2019; Fisher et al. 2020b; Wang et al. 2022).

In this study, we focus on the chemical behaviour of multiple accessory minerals from rocks collected along the metamorphic gradient of the Chugach Metamorphic Complex (CMC) in Alaska. These rocks record metamorphic conditions that range from greenschist (~500 °C) to upper amphibolite facies, reaching anatexis under water-saturated conditions (and minor muscovite breakdown) at 650–700 °C (Bruand et al. 2014). We present new major and trace element data of the main accessory phases (apatite, monazite, allanite and titanite) in samples collected in two transects along the metamorphic gradient as well as Sm–Nd isotope systematics in allanite, monazite and bulk-rock. We particularly demonstrate the capacity of apatite and monazite REE chemistries to track temperature increase up to anatexis within a limited temperature window of about ~150 °C. We also discuss the significant role of the bulk chemical composition in the stability of accessory phases and in their chemical variations, and highlight the Nd isotopic homogeneity of monazite and allanite across this metamorphic sequence.

Geological setting

Along the southern margin of Alaska, the Pacific plate subducts under the North American plate. This subduction system, active intermittently since the Jurassic, has led to the accretion of several terranes, including the Cretaceous-Paleogene Chugach terrane. The Chugach terrane is separated from the Wrangellia terrane to the north and the Prince William-Yakutat terrane to the south by a complex network of transform faults and thrusts (Fig. 1a). The Chugach terrane consists of an accretionary prism extending over

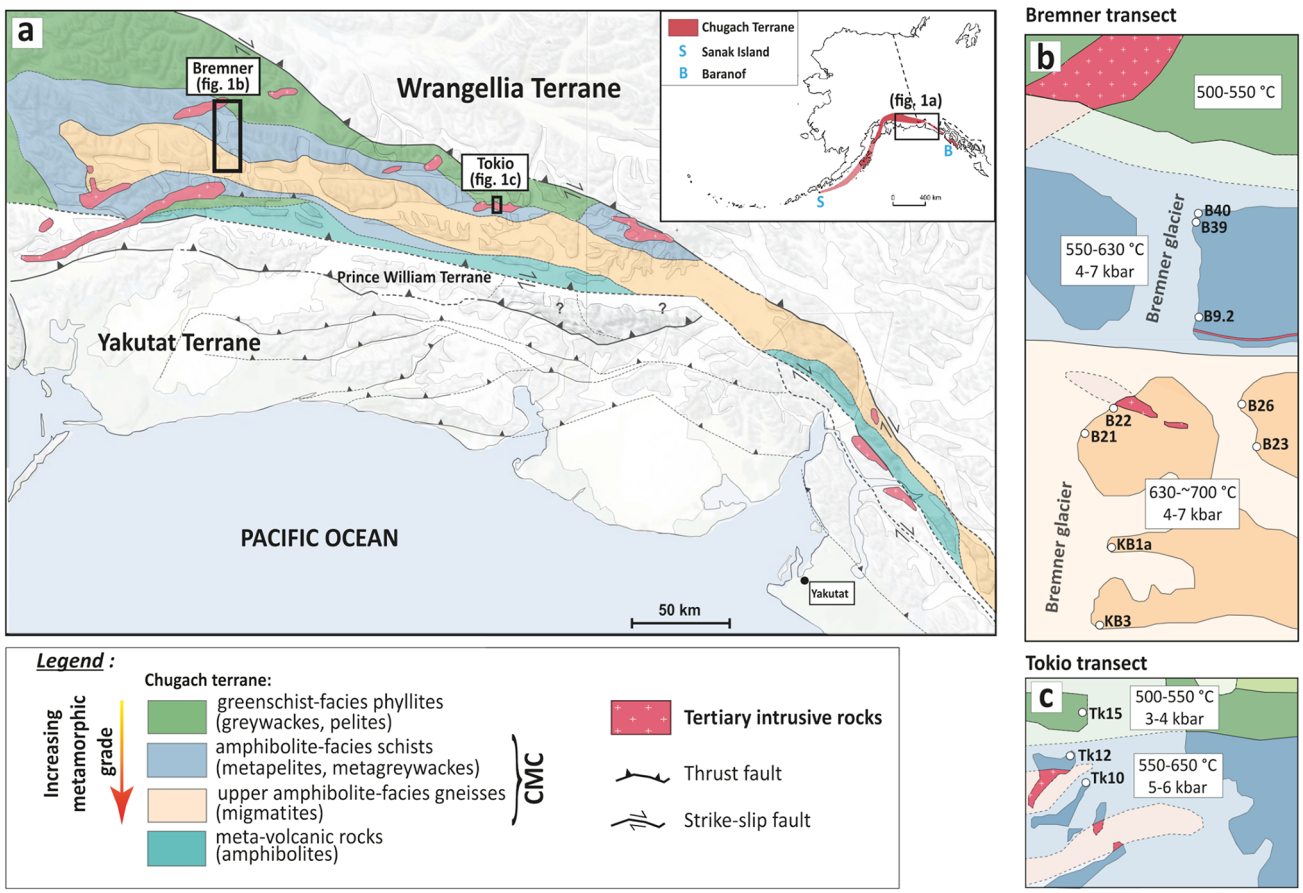

Fig. 1 Simplified geological map of the Chugach Metamorphic Complex (CMC) and surrounding terranes. **a** Overview of the study area with location of the Bremner transect and the Tokio transect; **b**, **c** geological maps of the Bremner and Tokio transects with sampling locations and indication of the *P-T* conditions determined by Bruand et al. (2014). Maps modified from Gasser et al. (2011)

2000 km along the Alaskan peninsula from Sanak Island to Baranof Island. This accretionary prism is primarily made of metapelites intercalated with metagreywackes (e.g. Sisson et al. 1989; Bruand et al. 2014). These sediments experienced Low Pressure-High Temperature (LP-HT) metamorphism ranging from zeolite-prehnite pumpellyite facies to (upper)-amphibolite facies (e.g. Hudson and Plafker 1982; Sisson et al. 1989; Dusel-Bacon 1994; Bruand et al. 2014). The Chugach Metamorphic Complex *s.s.* comprises two zones: the schist zone (amphibolite facies), which did not experience partial melting, and the migmatitic gneiss zone (upper amphibolite facies), which underwent crustal anatexis. Pseudosection modeling and petrographic observations show that partial melting occurred under water-saturated conditions at ~650–700 °C following the reaction $Pl + Qz + H_2O = melt$ (Bruand 2010; Bruand et al. 2014). Several thermobarometric studies on the Chugach terrane indicate an increase in *P-T* conditions from north to south, starting at 400–550 °C and < 4 kbar in the phyllite zone, rising to ~500–650 °C and ~3–7 kbar in the schist zone, and reaching ~650–750 °C and 4–13 kbar in the gneiss zone (Sisson et al. 1989; Bruand et al. 2014). U-Pb geochronological studies on zircon and monazite (Gasser et al. 2012a, b) indicate that metamorphism occurred over a relatively short time span in the Eocene (55 – 51 Ma), possibly due to the subduction of a spreading ridge (e.g. Bradley et al. 2003; Scharman et al. 2012). This metamorphic event was followed by rapid cooling and exhumation in the western and central parts of the complex, with slower cooling in the southeastern part (Gasser et al. 2011, 2012b). The granitoid intrusions of the Sanak-Baranof belt, coeval with the HT metamorphism, have been dated at 50–61 Ma (e.g. Bradley et al. 2003; Sisson et al. 2003).

Sample selection

For this study we selected twelve samples from two N-S transects: the Bremner and Tokio transects (Fig. 1), previously characterised for petrography and *P-T* conditions by Gasser et al. (2012b) and Bruand et al. (2014). The Bremner transect extends over approximately 20 km and crosses

from north to south: the phyllite zone (515–550 °C, 2–3 kbar), the schist zone (600–630 °C, 6.1–6.4 kbar), and the migmatitic gneiss zone (630 to ~700 °C, 4.4–6.1 kbar; Bruand et al. 2014). Located 100 km to the east, the Tokio transect (10 km from north to south) crosses the phyllite and schist zones (550–650 °C, 3–6 kbar; Bruand et al. 2014). These transects are locally crosscut by granitoid intrusions.

This selection is representative of the chemical diversity of the CMC. To investigate the potential effect of bulk rock compositions on the stability and chemistry of accessory phases, we selected both pelitic and greywacke samples. Previous petro-geochemical studies (microprobe and bulk major elements) were conducted on these samples (Gasser et al. 2012b; Bruand et al. 2014). *P-T* conditions along the studied transects were derived from various methods such as garnet-biotite thermometry, Raman spectroscopy on carbonaceous material (RSCM) and THERMOCALC modelling (Bruand et al. 2014). All in-situ analyses were acquired on thin sections, as macroscopic samples are no longer available.

Petrography, chemistry and *P–T* conditions

On the N-S oriented Bremmer transect, we selected three schist samples (B39, B40, B9.2), and six migmatitic gneiss samples (B21, B22, B23, B26, KB1a, KB3; Fig. 1b). Temperature inferred for these nine samples range from 600 to ~700 °C (Table 1). All gneisses have underwent partial melting in water-saturated conditions (±muscovite breakdown; Bruand et al. 2014). In the N–S Tokio transect, we studied one phyllite sample (Tk15) and two schist samples (Tk10 and Tk12) to gather complementary information on the phyllite and schist zones (Fig. 1c). The major element chemical compositions show that the analysed samples are close to the average pelite composition of Shaw (1956) but with a slightly higher CaO content, as already noted by Gasser et al. (2012) (Supplementary Table A1; Supplementary Fig. A2). When compared to the pelite average composition recently established by Forshaw and Pattison (2023), they have higher CaO and Na_2O contents and lower Al_2O_3 and K_2O contents (Supplementary Fig. A2). In the Bremner transect, the migmatitic samples B21 and KB3 lack aluminosilicate and garnet, and have a more greywacke-like composition with higher SiO_2/Al_2O_3 ratios (~4.5) than other gneisses (Supplementary Table A1; Gasser et al. 2012b). KB1a, which has garnet but contains almost no sillimanite, has an intermediate composition between metapelite and metagreywacke with SiO_2/Al_2O_3 ratio of 4.1.

The petrology of the studied samples is briefly described below, from the phyllite zone to the migmatitic gneiss zone.

The phyllite sample Tk15 has a quartz-plagioclase-biotite-muscovite-chlorite-epidote paragenesis and contains accessory minerals apatite, allanite, zircon and ilmenite (Gasser et al. 2012b; Table 1; Fig. 2a). This sample reached a peak temperature of about 530 °C in the greenschist facies (Bruand et al. 2014).

The three schist samples from the Bremner transect (B39, B40, B9.2) reached temperatures of about 600–630 °C and have a peak mineral assemblage of quartz-plagioclase-biotite-garnet-sillimanite. Chlorite and muscovite can appear as retrograde phases while apatite, monazite, xenotime, zircon and ilmenite are the main accessory phases (Gasser et al. 2012b; Bruand et al. 2014; Table 1; Fig. 2b, c). In the Tokio transect, the two schist samples Tk10 and Tk12 have a similar mineralogical composition to those of Bremner transect, except for the presence of large andalusite porphyroblasts instead of sillimanite (Bruand et al. 2014). They reached peak temperatures of ~620 and ~550 °C, respectively (Table 1).

The six-studied migmatitic gneisses (B21, B22, B23, B26, KB1a and KB3) equilibrated at temperature conditions ranging from 630 to ~700 °C. Pseudosection modelling on two samples showed that their peak temperatures could even have reached up to 750 °C (Bruand et al. 2014; Table 1). Their peak metamorphic assemblage includes quartz-plagioclase-biotite ± garnet ± sillimanite ± muscovite, with slight mineralogical variations mainly driven by bulk rock composition. For instance, sillimanite and garnet are absent in the metagreywacke samples (B21 and KB3; Bruand et al. 2014; Table 1; Fig. 2e, f). Common accessory phases in these rocks are apatite, monazite, xenotime, zircon, ilmenite (± epidote/allanite-titanite). Chlorite and muscovite appear as retrograde phases (Gasser et al. 2012b; Table 1; Fig. 2d–f). These rocks exhibit a strong foliation contemporaneous with migmatite development, with increasing migmatisation towards the south (Bruand et al. 2014). Following the terminology of Sawyer (2008), these rocks are metatexites formed from relatively low degree of partial melting. They consist of very fine layering of leucosomes (made up of 99% quartz and plagioclase and extremely rare K-feldspar; Bruand 2010) and mesosomes. Some more melanocratic layers are interpreted as residuum formed after subsequent melt extraction (Gasser 2010).

Analytical techniques

Image acquisition

Thin sections scans and BSE images were acquired using a Scanning Electron Microscope (SEM) Thermofisher (formerly FEI) QUANTA 200 with an accelerating voltage of 20 keV equipped with an EDS Oxford XMAX 80 detector in Brest, France. Images were processed using the Oxford

Table 1 Summary of mineralogical content (rock–forming minerals and accessory phases; Gasser et al. (2012b) and this study) and estimates of *P-T* conditions

Transect	Tokio transect			Bremner transect								
Sample	TK15	Tk10	Tk12	B39	B40	B9.2	B21*	B22	B23	B26	KB1a	KB3*
Latitude (°N)	60.6965	60.682	60.6878	60.8858	60.8883	60.8583	60.8124	60.8124	60.811	60.8236	60.7643	60.738
Longitude (°W)	141.5739	141.5716	141.5807	143.2384	143.2384	143.2362	143.3148	143.3148	143.1923	143.2033	143.2881	143.3014
Metamorphic zone	phyllite	schist	schist	schist	schist	schist	migmatitic gneiss	migmatitic gneiss	migmatitic gneiss	migmatitic gneiss	migmatitic gneiss	migmatitic gneiss
Mineralogy												
Rock-forming (+Qz-Pl-Bt)	Ms-Chl-Ep	And-Ms-Grt (Chl)	And-Ms-Grt	Grt-Sil-Ms	Grt-Sil-Ms	Grt-Sil-Ms	Ms	Grt-Sil	Grt-Sil	Grt-Sil-Ms	Grt-Ms (Sil, Kfs)	(Chl, Ms)
Mnz		x	x	x	x	x	x	x	x	x	x	x
Xtm		x	x	x	x	x	x	x	x	x	x	x
Ap	x	x	x	x	x	x	x	x	x	x	x	x
Ep/Aln	x	x	x			x	x		x		x	x
Zrn	x	x	x	x	x	x	x	x	x	x	x	x
Ilm	x	x	x	x	x	x	x	x	x	x	x	x
Ttn							x				x	x
Sulf		x		x	x	x	x	x	x	x	x	x
Fe-ox	x	x	x	x	x	x	x	x	x	x	x	x
P-T conditions												
T(°C)	526 ± 50[a]	620 ± 73[b]	543 ± 23[b]	597 ± 50[a]	597 ± 50[e]	632 ± 30[c]	~ 650[e]	623 ± 30[c] ~ 750[d]	645 ± 30[c]	628 ± 30[c]	645 ± 30[c] ~ 750[d]	666 ± 30[e]
P(kbar)		5.1 ± 2.9[b]	3.4 ± 0.9[b]			6.8 ± 1.6[b]		4.7 ± 1.9[b]		5.6 ± 2[b]	4.7 ± 1.6[b]	5.1 ± 1.6[e]

[a]RSCM

[b]Average *P-T* from THERMOCALC

[c]Bt-Grt thermometry

[d]Pseudosection modelling

[e]Geothermobarometers not available. In this case, *P-T* values are taken from samples in their vicinity

*Greywacke samples

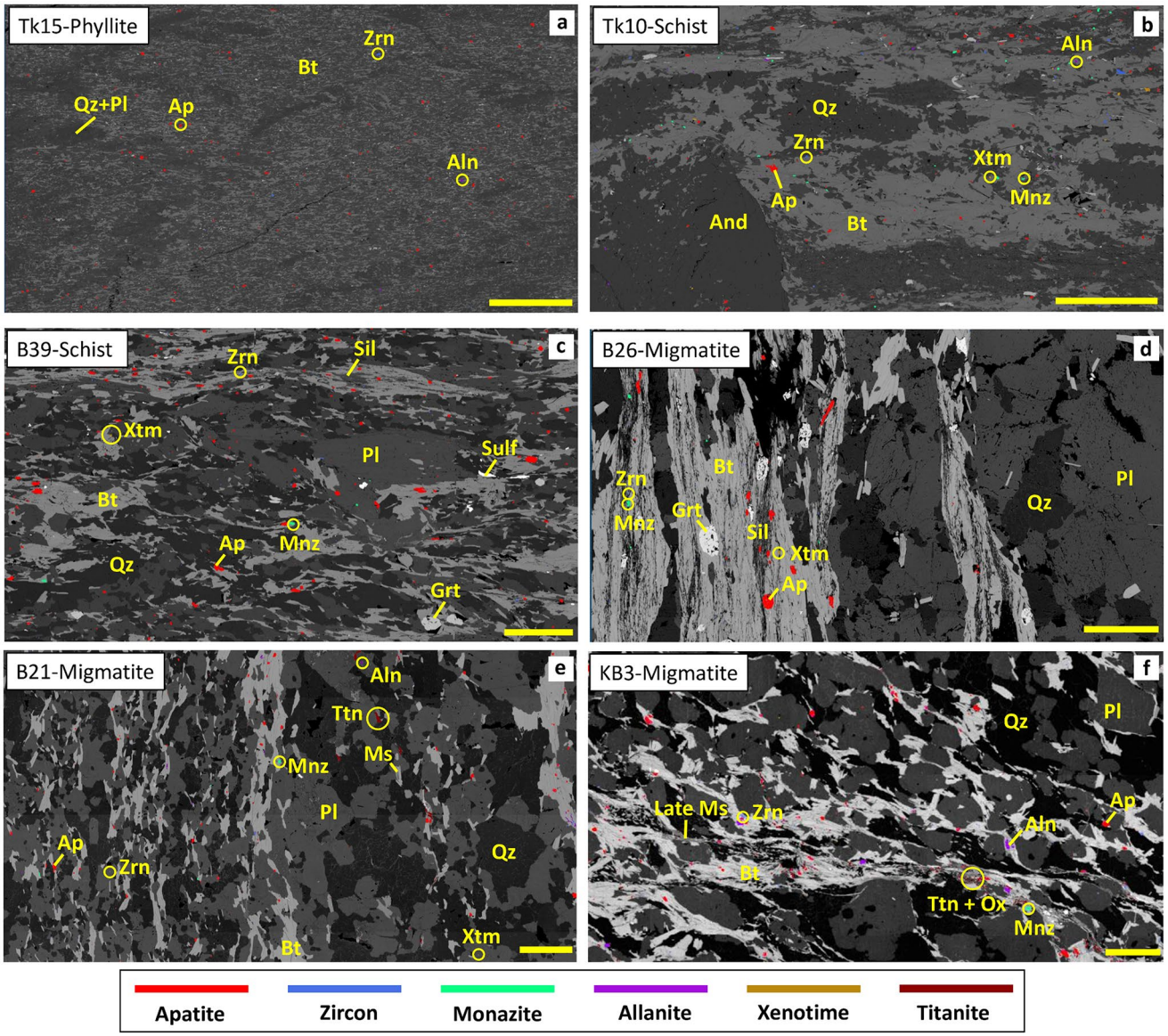

Fig. 2 Representative backscattered (BSE) photomicrographs of selected CMC samples in thin sections (phyllite (**a**); schists (**b**, **c**) and migmatitic gneisses (**d**–**f**)) indicating mineral assemblages and detected accessory phases by AZTEC software: apatite in red, zircon in blue, monazite in green, allanite in purple, xenotime in gold and titanite in dark red. Yellow scale bar = 1 mm. Mineral abbreviations used in the paper are from Whitney and Evans (2010)

Aztec software and accessory minerals were located using the "Particle mode". Statistical data on grains proportion and size were also obtained using this mode. Further images processing was done using ImageJ software (Schneider et al. 2012). Each accessory phase was then imaged using a BSE detector. Cathodoluminescence (CL) images of apatite were done with a KeDev Centaurus CL detector housed on a JEOL JSM-5910LV SEM (accelerating voltage: 15 keV) at the Laboratoire Magmas et Volcans (LMV) in Clermont-Ferrand, France.

Electron probe microanalysis (EPMA)

Major element concentrations in accessory phases were determined using the LMV CAMECA SX Five-Tactis microprobe and the CAMECA SX 100 microprobe from the Microsonde Ouest laboratory (Brest, France). Apatite and monazite analyses were done with an accelerating voltage of 20 keV and a beam current of 20 nA. For apatite, LLIF crystal was used for Fe and Mn, PC0 was used for F, TAP was used for Si, Sr, Y and LPET was used for Ca, P and Cl. For monazite, LLIF crystal was used for Pr, Nd, Sm, Gd, TAP was used for Si and Y and LPET was used for P, Ca,

Ce, La and Pb. Some xenotime grains were also analysed with the same program as monazite. For titanite and allanite, analyses were done with an accelerating voltage of 20 keV and a beam current of 40 nA, using LLIF crystal for Fe and Nd, PC0 for F, TAP for Si, Al, Y and LPET for Ca, Ti, La. For apatite and allanite, a defocused beam of 5 µm was applied to avoid migration effects described for halogens (F, Cl; Pyle et al. 2002).

Laser ablation inductively coupled plasma mass spectrometry (LA-ICP-MS)

Trace element contents of accessory minerals were analysed by LA-ICP-MS using the LMV Thermo Element XR mass spectrometer coupled with the 193 nm Resonetics Resolution M-50E laser. Each analysis consisted of 25 s of background acquisition and 85 s of ablation. The diameters of the laser beam were 15 or 20 µm for apatite and allanite, 9, 12 or15 µm for monazite (depending on their size), and 20 µm for titanite. The ablation frequency was set at 1 Hz and the fluence at 2.7 J/cm^2. A sample bracketing method was used, treating USGS glass GSE-1G (Jochum et al. 2005) as primary standard to calculate elemental concentrations and to correct instrumental drift. Internal standard element used for data normalisation was ^{43}Ca for apatite, allanite and titanite, and ^{140}Ce for monazite, obtained by EPMA. USGS glass GSD-1G (Jochum et al. 2005) was used as a secondary standard to check data robustness, reproducing certified values to within 10% for all elements (Supplementary Table B6). Natural standards Durango apatite (Marks et al. 2012) and Bananeira monazite (Gonçalves et al. 2016) were regularly analysed with the same parameters to control the quality of the data (see details in Supplementary Table B6). Data processing was carried out using GLITTER software (Griffin et al. 2008). Additional data and parameters on the LA-ICP-MS system can be found in Supplementary Table B7.

In situ Sm–Nd measurement in monazite and allanite

Among the twelve samples studied, seven samples were selected for in-situ Sm–Nd analysis in monazite and allanite. Analyses were acquired during two sessions on the LMV Thermo Fisher Scientific™ Neptune Plus™ mass spectrometer coupled with the 193 nm Resonetics Resolution M-50E laser using the procedure described in Doucelance et al. (2020). Only monazite and allanite have been analysed as their size and Nd contents permitted satisfactory analyses. Although ubiquitous in our samples, the apatite grains were generally too small and did not contain enough Nd (< 500 ppm). The first 20 cycles of every measurement were used to evaluate the baseline level of each Faraday Cup. Each analysis consisted of 90 measurement cycles. Depending on the run, a spot size of 9, 15 or 20 µm was used for monazite and 15, 20, 27 or33 µm for allanite. The laser was set to a frequency of 4 Hz and energy fluence to 3.4 J/cm^2. Helium and N_2 flow rates were 725–825 ml/min and 3.4–3.8 ml/min respectively, depending on the sessions. Other analytical parameters are given in Supplementary Table C6. The oxide level (ThO^+/Th) at the beginning of the session was always < 15%, decreasing during the session to avoid a ^{145}Nd/^{144}Nd drift, as described by Fisher et al. (2020a). JNdi-1 doped glass was analysed regularly during the sessions to monitor potential instrumental drift (Fisher et al. 2011; Doucelance et al. 2020). Primary standards STK for monazite (^{143}Nd/^{144}Nd = 0.511895; Fisher et al. 2020a) and Connecticut for allanite (^{143}Nd/^{144}Nd = 0.512106; Wang et al. 2022) were analysed regularly under the same conditions as the unknowns, and were used for normalisation and instrumental drift correction when necessary (Supplementary Tables C2-3). Gale allanite (^{143}Nd/^{144}Nd = 0.512999; Wang et al. 2022) and Trebilcock monazite (^{143}Nd/^{144}Nd = 0.512616; Fisher et al. 2011) were used as secondary standards for quality control (Supplementary Tables C4-5). A value of ^{145}Nd/^{144}Nd = 0.348415 (Wasserburg et al. 1981) was used as a reference for internal quality control of the analyses. Primary and secondary standards analysed within the same sequence and under the same parameters yielded means that matched published reference values within uncertainties (2SE) (Supplementary Table B2-5).

Whole-rock Sm–Nd analysis

Neodymium isotopic measurements were performed on seven samples (five gneisses and two schists) for which in-situ Sm–Nd measurements on monazite or allanite were also acquired. For whole-rock measurements, 100 mg of powder was dissolved in Teflon vials using the NH_4HF_2 to ensure the dissolution of refractory minerals such as zircon (Zhang et al. 2012). This mixture was then heated at 220°C for 48 h. AGV-2, BHVO-2 and GSP-2 standards were used and followed the same experimental protocol. The separation of Nd was done using the "cascade" column protocol of Pin et al. (1994). The samples were first loaded on AG50-X4 columns for removing iron. Then, the samples were loaded into the TRU Spec resin columns for collecting REE and U. Finally, the remaining fraction was processed through the Ln Spec resin columns to collect Nd and remove Sm that produces isobaric interference on masses 144, 148, 150. Procedure blanks were < 50 pg for Nd. The samples were taken up with 2 mL of HNO_3 0.05 N. Then a dilution was carried out to obtain solutions of 300 ppb. The data were acquired on the LMV Thermo Fisher Scientific™ Neptune Plus™ MC-ICP-MS using a static collection. Repeated

measurements of JNdi-1 ppb standard during the session gave $^{143}Nd/^{144}Nd = 0.512091 \pm 10$ (2SD, n = 8), which is consistent with the value of 0.512099 ± 5 measured using a dynamic routine (Garçon et al. 2018). AGV-2, BHVO-2 and GSP-2 standards gave respectively $^{143}Nd/^{144}Nd = 0.512760 \pm 8$ (2SE), 0.512987 ± 8 (2SE) and 0.511366 ± 7 (2SE) and are consistent with published values reported in the GEOREM database.

Results

Accessory minerals petrography

The accessory minerals observed in the studied samples are zircon, apatite, monazite, xenotime, allanite and titanite. Ilmenite, sulfur and Fe-oxide are also present but were not studied in this contribution.

Apatite is present in all the analysed samples. Its maximum size increases with metamorphic grade, reaching 50 µm in the phyllite (Fig. 3a), 100 µm in the schist (Fig. 3c) and > 200 µm in the gneiss zones (see also Supplementary Table A2). The backscattered electron (BSE) and cathodoluminescence (CL) images do not show any obvious zoning except in the metagreywacke samples (B21 and KB3), where dissolution-reprecipitation features were observed, consisting of the individualisation of up to three concentric zones separated by a lobate-cuspate interface (Fig. 3i; 7a; Supplementary Fig. A1e). Most apatite grains from the migmatitic gneiss zone are enclosed in the biotitic framework, with a small number of grains (10–15%) found in the leucosome. Apatite also appears as a destabilisation product

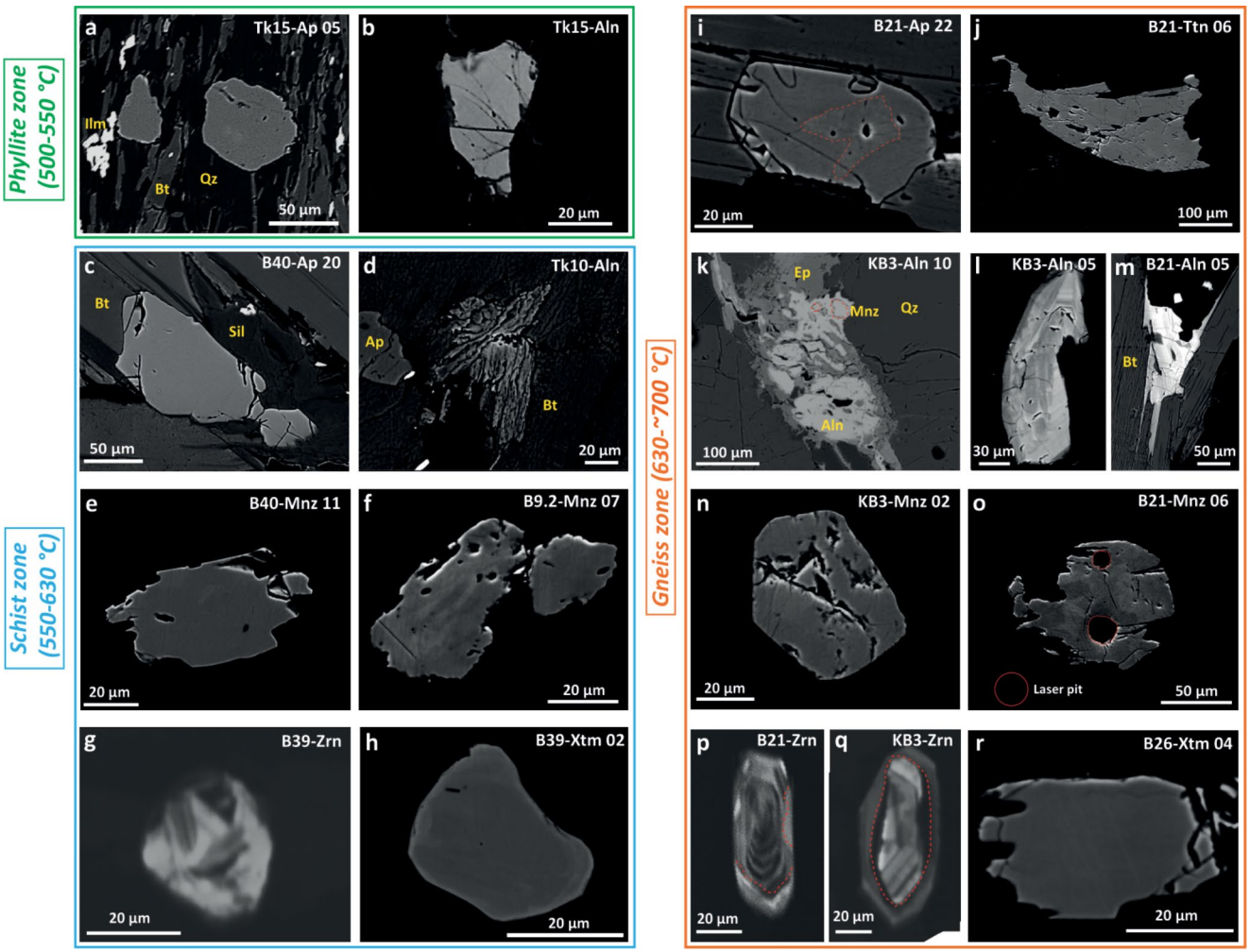

Fig. 3 Petrographic features of some representative accessory phases along the metamorphic gradient: BSE images of phyllite zone apatite (**a**) and allanite (**b**); schist zone apatite (**c**), allanite (**d**), monazite (**e**, **f**) and xenotime (**h**); migmatitic gneiss zone apatite (**i**) with core-rim textures observed in B21, titanite (**j**), allanite (**k**–**m**), monazite (**n**, **o**) and xenotime (**r**). Cathodoluminescence images of zircon from schist zone (**g**) and migmatitic gneiss zone (**p**, **q**). The latter shows an oscillatory-zoned core and a thin unzoned rim (< 15 µm) highlighted by the red dashed line. When indicated, grains number refers to in-situ analyses that can be found in Supplementary Materials B and C

of monazite, rimming or forming coronae around monazite grains (Supplementary Fig. A1a).

Monazite is present in all samples, except in the phyllite (Gasser et al. 2012b). The grains are often small, particularly in the schist zone (often < 25 µm; Fig. 3e, f), but can reach up to 50 µm in some migmatitic gneisses (e.g. B21 or KB3; Fig. 3n, o). In gneisses, monazite can be found as inclusions in biotite or in leucocratic quartzo-feldspathic zones (Fig. 2d, e, f). Occasionally, some samples (e.g. KB3) show allanite-epidote ± apatite coronae around monazite, interpreted as a destabilisation texture along the retrograde path (Gasser et al. 2012b; Supplementary Fig. A1a). Monazite grains are generally homogeneous in BSE images (Fig. 3e, f, n), despite some grains occasionally revealing patchy zoning (Fig. 3o). Unlike the results on separated grains presented in Gasser et al. (2012b), no core-to-rim zoning in monazite from the studied migmatitic gneisses thin sections was clearly observed.

Small allanite crystals (< 20 µm) are present in the phyllite zone (Tk15). They are homogeneous in BSE images and are sometimes broken (Fig. 3b). They are interpreted as detrital grains by Gasser et al. (2012b). They are absent in the schists of the Bremner transect (allanite to monazite breakdown reaction; Gasser et al. 2012b), but were identified in the schists of the Tokio transect (sizes from 20 to 40 µm) as fibrous crystals in biotite cleavages (Fig. 3d). In most of the migmatitic gneisses, allanite is rare and forms small crystals (often < 50 µm in size) preferentially located in biotite cleavages (Fig. 3m), and is seldom associated with epidote that most likely formed during the retrograde history (Gasser et al. 2012b). In the greywacke gneisses (B21, KB3), two other types of allanite are found: either as large crystals (up to 200 µm; Fig. 3l), often located in quartzo-feldspathic domains or in zones of late fluid circulation, occasionally associated with titanite and iron oxide (KB3; Fig. 2f). They are also found associated with epidote, forming coronae around monazite (Fig. 3k; Supplementary Fig. A1a) and xenotime (Supplementary Fig. A1b), and interpreted as retrograde alteration textures (Gasser et al. 2012b). BSE images often show rather homogeneous grains (Fig. 3l, m), and occasionally patchy zoning (e.g. KB1a, B23).

Titanite only appears in three samples of the migmatitic gneiss zone (B21, KB1a and KB3). Crystals are generally smaller than 100 µm (KB1, B21; Fig. 3j). In B21, the grains are euhedral and are often located in the quartz-feldspathic matrix (leucosome) and more rarely associated with biotite (Fig. 2e; Supplementary Fig. A1g). In sample KB3, very small anhedral crystals (10 µm) appear in the vicinity of iron oxide-rich late fluids circulation pathways in biotite cleavages (Fig. 2f). In sample KB1a, grains are smaller than 50 µm and located in biotite cleavages. Titanite grains are homogeneous in BSE imaging in all the samples (Fig. 3j).

Xenotime is present in all schists and gneisses samples, but in small quantities, generally with fewer than ten grains per thin section. It often forms small, rounded crystals (< 20 µm) mainly located in the biotite framework. In the metagreywacke samples (B21 and KB3), some grains are also included in feldspar or located along quartz-feldspar boundaries in the quartzo-feldspathic zones. In KB3, xenotime is scarce (three grains) but reaches larger sizes (up to 100 µm). In BSE images, the grains are homogeneous (Fig. 3r) though some can exhibit patchy zoning or lighter BSE rims (e.g. B39; Fig. 3h or KB3; Supplementary Fig. A1c). Associations with apatite or zircon can sometimes be observed (Supplementary Fig. A1d).

Zircon appears in all the studied samples. In the phyllite and the schists, the grains are small (< 30 µm), rounded (Fig. 3g) or elongated with oscillatory, patchy or sector zoning. In the migmatitic gneisses, rounded and prismatic grains are present, with sizes reaching up to 100 µm. In CL, they show a typical core-rim texture with oscillatory, patchy or sector zoned cores and lighter unzoned rims (Fig. 3p, q; see also Gasser et al. 2012a). In most samples, crystals are found enclosed in biotite and more rarely associated with feldspar or quartz.

Accessory phases major and trace elements

Chemical data for apatite, monazite, allanite and titanite in samples from both transects are presented in Supplementary Tables B1-4 and are described below. Our focus is on the description of the REE contents and Nd isotopes signatures of these phases. Other major and trace elements are presented and discussed when appropriate. Few microprobe data have been acquired on xenotime grains but no clear trends were observed between metamorphic grade and their chemistry (Supplementary Table B5). Due to their small size (< 20 µm), xenotime grains could not be analysed by LA-ICP-MS, and their chemistry will not be further discussed.

Apatite chemistry

The major element contents of apatite throughout the samples show significant variation in CaO and P_2O_5 contents, ranging between 51.9 and 55.8 wt% and 39.8–42.8 wt%, respectively. The fluorine (F) content in apatite varies between 2.39 and 3.16 wt% in the phyllite zone and ranges from 2.36 to 4.21 wt% in the schist zone to 2.43–3.95 wt% in the migmatitic gneiss zone (Fig. 4a). We note that Cl is generally lower than 0.10 wt%, often close to or below detection limit (120 ppm), with the exception of the B40 sample where Cl content ranges between 0.13 and 0.49 wt%. All analysed apatite grains correspond to fluor-apatite, according to the classification by Palma et al. (2019).

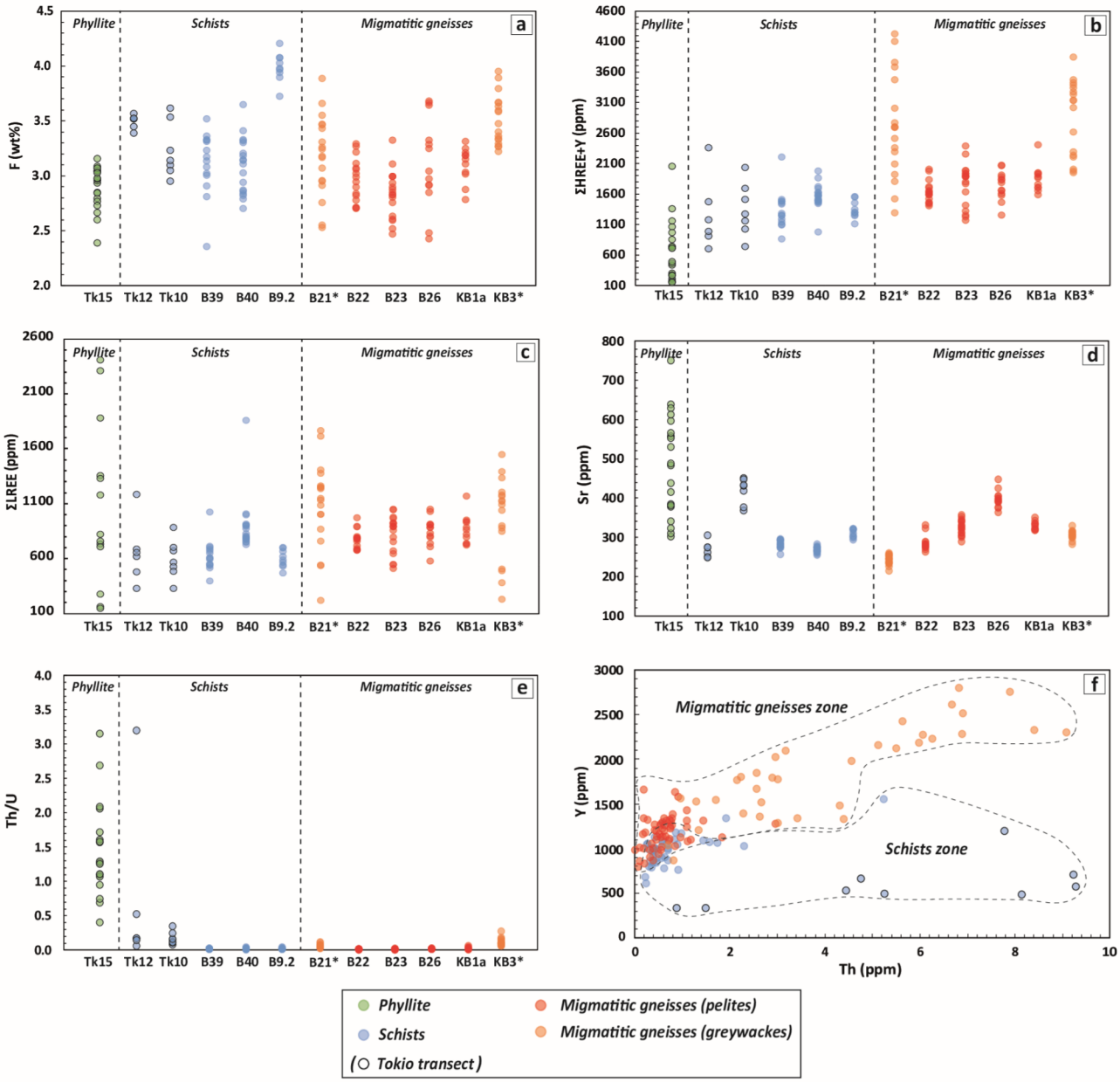

Fig. 4 Chemical evolution of **a** F (wt%), **b** ΣHREE-Y (Tb-Lu + Y in ppm), **c** ΣLREE (La-Nd in ppm), **d** Sr (ppm), and **e** Th/U for apatite along the metamorphic gradient. **f** Y (ppm) vs. Th (ppm) for apatite from schists and migmatitic gneisses. * = greywacke samples. Each point represents a single analysis

In the phyllite zone, Tk15 apatite grains exhibit relatively low HREE-Y contents compared to those in schists and gneisses (ΣHREE-Y (Tb to Lu + Y) = 153–2055 ppm; Fig. 4b). They also show highly variable LREE contents (ΣLREE (La to Nd) = 16.5–2407 ppm), Sr (302–750 ppm), and Th/U ratios (0.75–7.82; Fig. 4c, d, e). Chondrite-normalised REE patterns reveal negative Eu anomalies ranging from 0.31 to 0.73 ($Eu/Eu^* = Eu_N \sqrt{Sm_N * Gd_N}$), significant variations in LREE patterns (La/Sm_N = 0.12–1.94), and negatively sloped HREE pattern with Dy/Yb_N = 1.46–2.45 (Fig. 5a).

In the schist zone, apatite crystals HREE-Y contents range between 700 and 2358 ppm (Fig. 4b). The REE patterns of apatite in this zone show weak to strong negative Eu anomalies, ranging between 0.08 and 0.47 (Figs. 5a and 6a), depletion in LREE compared to MREE (La/Sm_N = 0.16–0.41), and a highly fractionated HREE spectra (Dy/Yb_N = 2.32–13.6; Figs. 5a and 6c). The Sr content varies

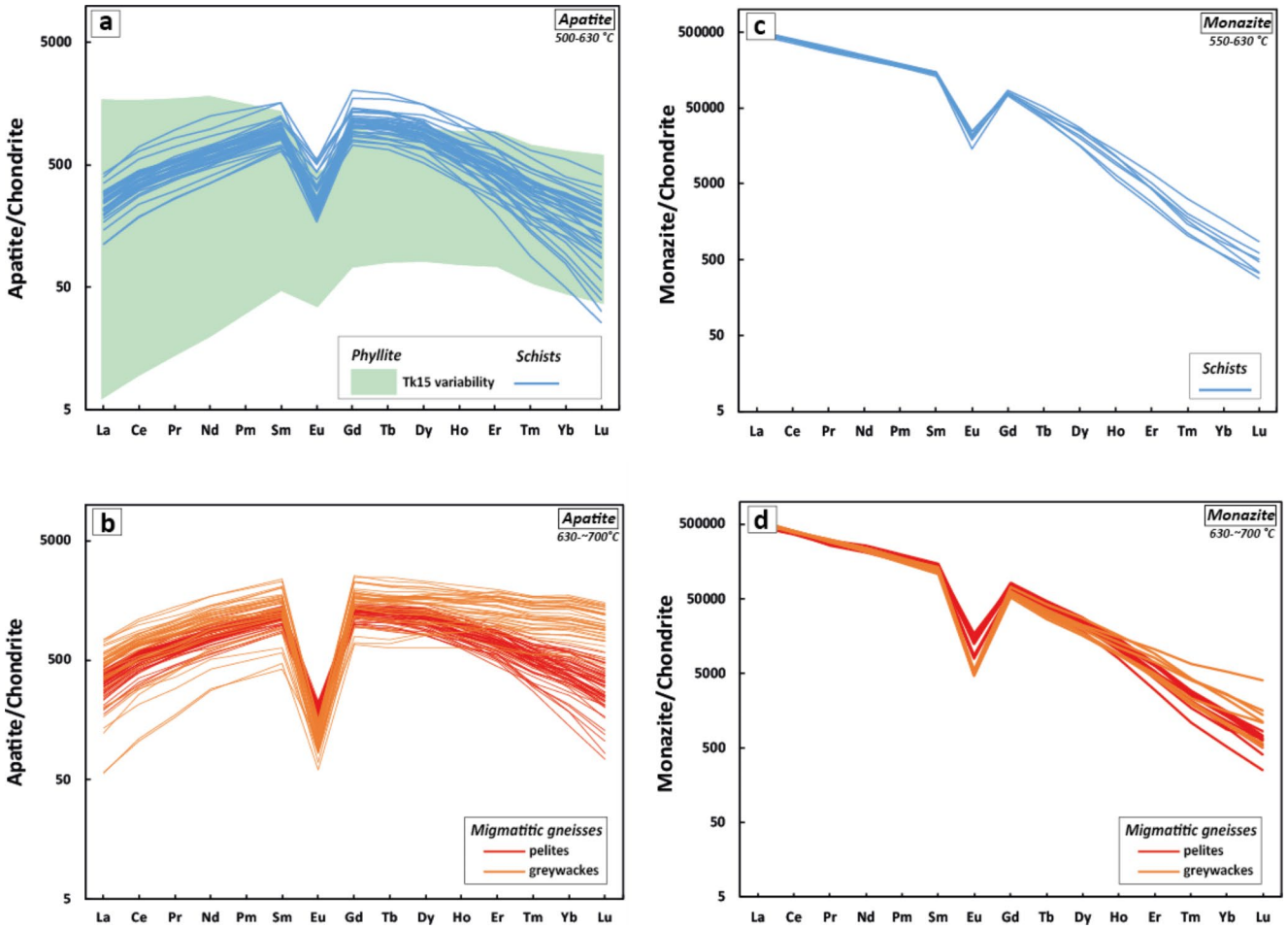

Fig. 5 Chondrite-normalised REE patterns of apatite for schists and Tk15 phyllite (**a**), and for migmatitic gneisses (**b**) and of monazite for schists (**c**) and for migmatitic gneisses (**d**). Normalising values of McDonough and Sun (1995). Temperature range of the samples are from Bruand et al. (2014)

between 247 and 450 ppm (Fig. 4d). Apatite grains in the schists of the Bremner transect show identical Th/U (~0.02) while those of the Tokio transect are notably characterised by higher Th contents, resulting in slightly higher Th/U ratios (0.06–0.52; Fig. 4e).

In the migmatitic gneisses, apatite grains of the metapelitic samples (B22, B23, B26, KB1a) have slightly higher HREE-Y contents than those in the phyllite and schist zones (ΣHREE-Y = 1173–2407 ppm; Fig. 4b). In these gneisses, their REE patterns show a generally strong negative Eu anomaly (average Eu/Eu* = 0.10–0.20; Figs. 5b and 6a). Apatite LREE patterns are similar to those in the schists (La/Sm_N = 0.20–0.35), while its HREE patterns are less depleted (Dy/Yb_N = 1.84–4.36; Figs. 5b and 6c). Apatite Sr content (214–448 ppm) and Th/U ratios (0.01–0.06) in these gneisses are comparable to those in the schists (Fig. 4e). Apatite from the metagreywackes B21 and KB3 shows a flat pattern for HREE-Y (Dy/Yb_N ratios = 0.84–1.52 and ΣHREE-Y = 1294–4225 ppm) and slightly stronger Eu anomalies when compared to other gneisses (Eu/Eu* = 0.06–0.20; Fig. 5b). Furthermore, apatite in these two samples is characterised by greater intra-grain REE-Y variability, which is positively correlated with Th (Fig. 4f) and U (Supplementary Table B1). This variability corresponds to the different zones (Z1-Z2-Z3) of the crystal showing dissolution-reprecipitation features observed in CL images (Fig. 7a). Microprobe transects across representative apatite grains of sample B21 show Y_2O_3-enriched zones (Z1-Z3; bright zones in CL) and Y_2O_3-depleted zones (Z2; dark zones in CL Fig. 7b).

Monazite chemistry

Monazite REE spectra from metapelitic schists and gneisses show a general strong enrichment in LREE (La/Sm_N = 3.15–4.04), a marked depletion in HREE (Dy/Yb_N = 14.6–36.5) and a negative Eu anomaly (Eu/Eu* = 0.09–0.23; Fig. 5c, d). A progressive increase in the intensity of the negative Eu anomaly is observed (average Eu/Eu* = 0.20 for schists

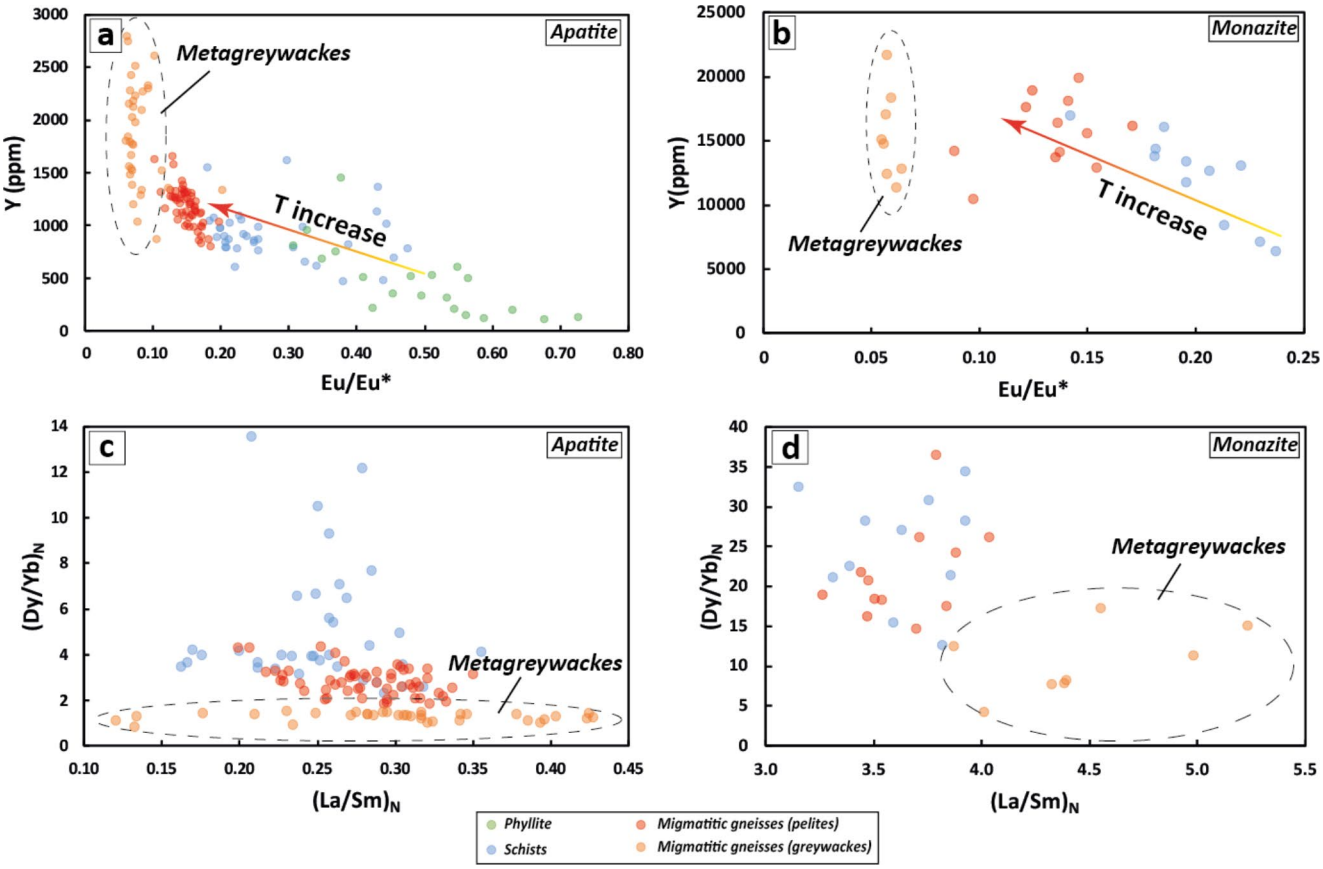

Fig. 6 Apatite and monazite geochemical features in the phyllite, schist and migmatitic gneiss zones. Eu/Eu* vs. Y content (ppm) for apatite (**a**) and monazite (**b**); $(Dy/Yb)_N$ vs. $(La/Sm)_N$ for apatite (**c**) and monazite (**d**). The arrow indicates increasing temperature up to anatexis while the dashed ellipse indicates the field of metagreywacke samples. Other samples are metapelites

vs. 0.13 for gneisses) along with an increase in HREE-Y content (average ΣHREE-Y = 2.03 wt% for schists vs. 2.43 wt% for gneisses; Supplementary Table B2) during the transition from schists to migmatitic gneisses for a pelitic composition (Fig. 6b). Monazite from migmatitic gneisses with greywacke compositions (B21 and KB3) displays distinct characteristics, with stronger negative Eu anomalies (Eu/Eu* = 0.06), less fractionated HREE patterns (Dy/Yb_N = 4.22–17.3), and slightly more enriched LREE patterns (La/Sm_N = 3.87–5.23; Figs. 5d and 6d) compared to monazite from other metapelitic gneisses.

Titanite chemistry

Titanite is only present in three gneisses (B21, KB1 and KB3) and shows rather homogeneous major element compositions with TiO_2 = 35.4–37.9 wt%, CaO = 27.5–28.6 wt% and Al_2O_3 = 1.64–3.19 wt%. The REE patterns vary significantly between these different samples and even between grains of each sample (e.g. ΣREE-Y = 32.2–3690 ppm for B21; Fig. 8a). For samples B21 and KB3, the REE patterns range from relatively flat to strongly enriched in HREE and depleted in LREE. Titanite also exhibits positive Eu anomalies (Eu/Eu* = 1.17-47.0 for B21). In KB1a migmatitic gneiss, only one titanite was analysed. This titanite is enriched in HREE relative to LREE and has a negative Eu anomaly (Eu/Eu* = 0.20). The Zr-in-titanite, used as a thermometer (Hayden et al. 2008), indicates temperature ranges between 596 and 727 °C (Supplementary Table B4), which is in good agreement with previous temperature estimates (Bruand et al. 2014).

Allanite chemistry

Allanite grains were only analysed in two gneisses (B21 and KB3). Their major element compositions range between 30.8 and 34.3 wt% for SiO_2, 16.8 and 22.1 wt% for Al_2O_3, 9.0 and 16.3 wt% for CaO, 8.0 and 11.5 wt% for FeO. They have a La/Ce atomic ratio of approximatively 0.5, classifying them as Ce-allanite (e.g. Gieré & Sorensen, 2004). Allanite REE spectra from these samples are similar, showing enrichment in LREE (La/Sm_N = 2.46–4.60) and depletion in HREE (Dy/Yb_N = 1.84–7.02; Fig. 8b). The Eu anomalies are negative but vary considerably between the different

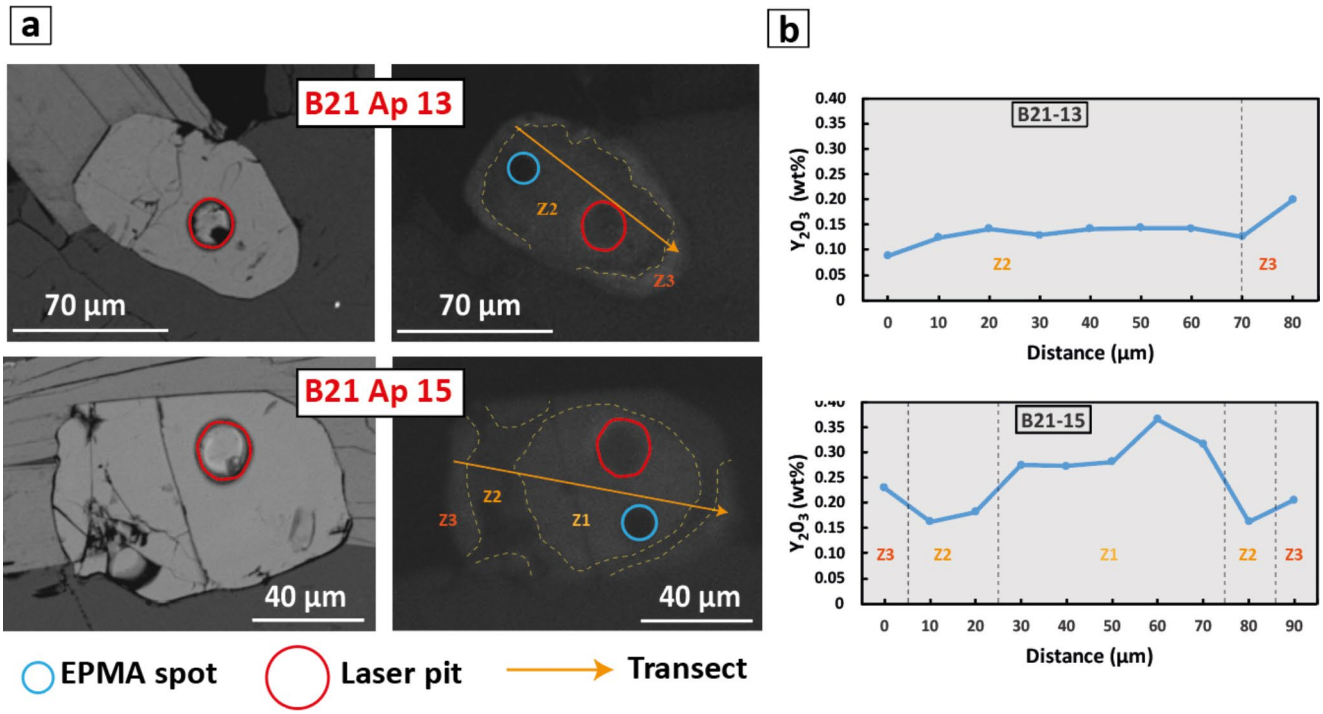

Fig. 7 Textural and yttrium zoning in apatite grains. **a** BSE (left) and cathodoluminescence (right) imaging of B21 migmatitic gneiss apatites. Dissolution-reprecipitation textures can be observed in the cathodoluminescence images. Up to two dissolution fronts (yellow dashed lines) and three zones (Z1, Z2, Z3) were recognised. EPMA and laser spots are indicated. **b** Y_2O_3 (wt%) transects (orange arrows) made by EPMA

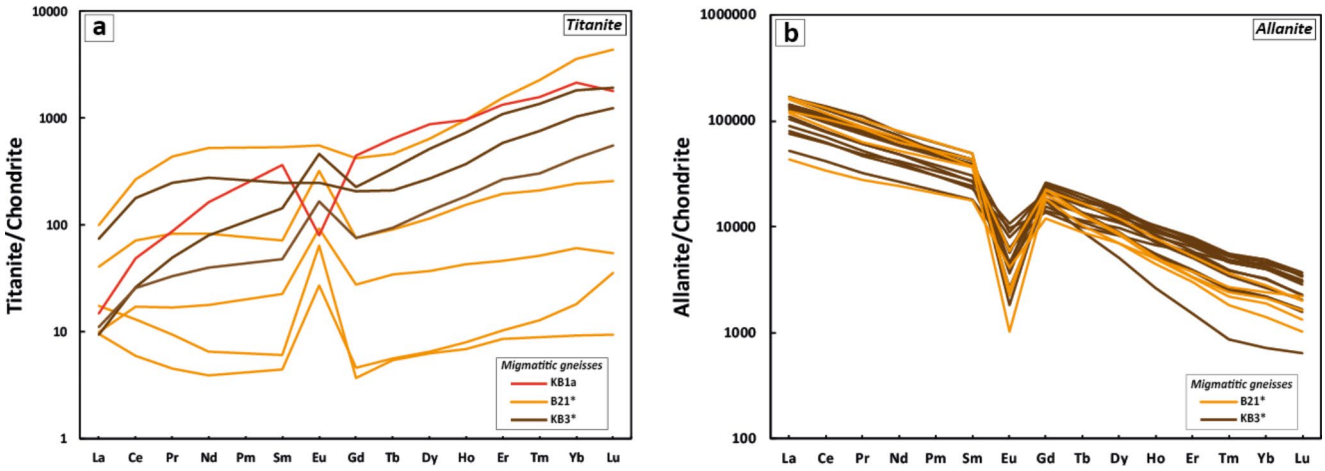

Fig. 8 Chondrite-normalised REE patterns of titanite (**a**) and allanite (**b**) for B21, KB1a and KB3 samples. Normalising values of McDonough and Sun (1995). * = metagreywacke samples

grains of a given sample (e.g. Eu/Eu* = 0.06–0.45 for KB3) and are positively correlated with the REE-Y content (Fig. 8b, Supplementary Table B3). Allanite grains from KB3 also have similar Th/U ranging between 2.5 and 6.2, while B21 allanite shows more variation with Th/U ranging from 0.44 to 15.1 (Supplementary Table B3). These low Th/U ratios, coupled with moderate enrichments in LREE and negative Eu anomalies, are typical of metamorphic allanite compositions (Gregory et al. 2012; Deng et al. 2014).

Nd isotopes analyses

The Nd isotopic compositions measured on bulk-rock and the mean value obtained for monazite and allanite are presented in Tables 2 and 3. Individual in-situ analyses are provided in Supplementary Table C1. Figure 9 illustrates the initial isotopic compositions ($\varepsilon Nd_{55\ Ma}$) of monazite and allanite along the metamorphic gradient.

Table 2 WR Nd isotopic composition with 2SE (internal uncertainty) and $^{147}Sm/^{144}Nd$ calculated from trace element measurements for the studied samples

Sample	Metamorphic zone	$^{143}Nd/^{144}Nd$	$^{147}Sm/^{144}Nd$	$(^{143}Nd/^{144}Nd)_{55\ Ma}$	2SE	εNd_{55Ma}	2SE
B39	schist	0.512446	0.1088	0.512406	0.000007	-2.99	0.25
B40	schist	0.512481	0.1041	0.512443	0.000006	-2.27	0.24
B21	migmatitic gneiss	0.512506	0.1008	0.512470	0.000007	-1.74	0.25
B23	migmatitic gneiss	0.512444	0.1127	0.512403	0.000006	-3.05	0.25
B26	migmatitic gneiss	0.512509	0.1122	0.512403	0.000006	-3.06	0.25
KB1a	migmatitic gneiss	0.512442	0.1249	0.512397	0.000006	-3.18	0.24
KB3	migmatitic gneiss	0.512489	0.1234	0.512445	0.000007	-2.61	0.26

The εNd were calculated using the decay constant $\lambda = 6.54.10^{-12}$ (Lugmair and Marti 1978), CHUR parameters from Bouvier et al. (2008) and an age of 55 Ma, corresponding to the age of metamorphism (Gasser et al. 2012a, b). Error propagations on the εNd were carried out using the spreadsheet from Ickert (2013).

Table 3 Average Nd isotopic composition and εNd_{55Ma} with 2SD for monazite and allanite in the studied samples. Details of the analyses can be found in Supplementary Table C1

Sample	Metamorphic zone	$(^{143}Nd/^{144}Nd)_{55\ Ma}$	2SD	εNd_{55Ma}	2SD	*n*
MONAZITE						
B39	Schist	0.512383	0.000085	– 3.44	1.66	6
B40	Schist	0.512423	0.000053	– 2.67	1.03	7
B21	Migmatitic gneiss	0.512460	0.000019	– 1.94	0.37	4
B23	Migmatitic gneiss	0.512409	0.000010	– 2.94	0.19	3
B26	Migmatitic gneiss	0.512457	0.000052	– 2.01	1.01	3
KB3	Migmatitic gneiss	0.512443	0.000046	– 2.28	0.90	4
ALLANITE						
B21	Migmatitic gneiss	0.512472	0.000113	– 1.70	2.10	7
B23	Migmatitic gneiss	0.512391	0.00012	– 3.29	2.04	2
KB1a	Migmatitic gneiss	0.512385	0.000098	– 3.40	1.91	6
KB3	Migmatitic gneiss	0.512436	0.000045	– 2.40	0.89	7

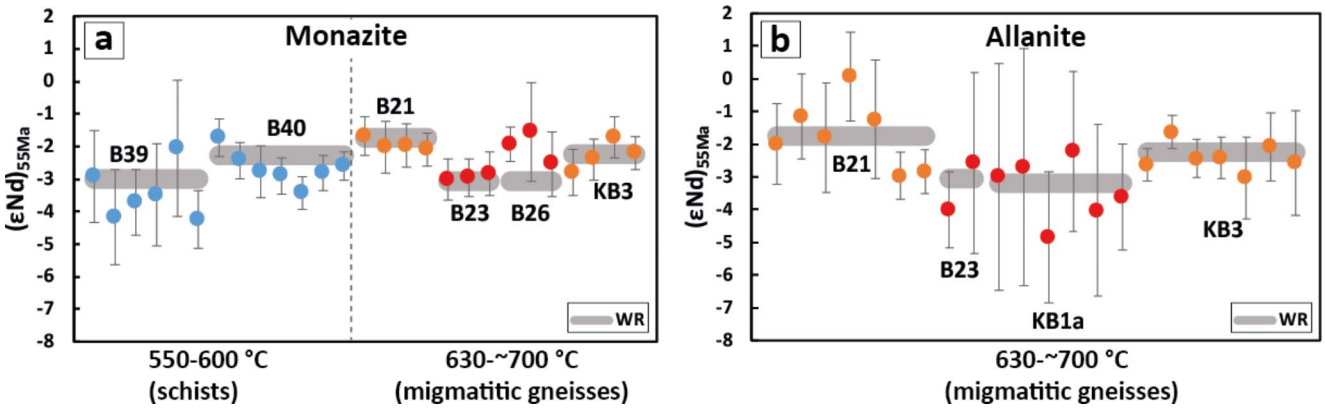

Fig. 9 Values of εNd_{55Ma} for monazite (**a**) and allanite (**b**) for schists and migmatitic gneisses samples along the metamorphic gradient. WR data are also shown (grey lines). The age of 55 Ma corresponds to the maximum age for metamorphism (Gasser et al. 2012a, b). Error bars are 2SE. Color-coding is the same as in Fig. 7

Across the transect, Nd isotopic compositions of both mineral species (allanite and monazite) show a remarkable homogeneity between the different grains of a given sample and between samples. Along the Bremner transect, εNd_{55Ma} for monazite grains range from -4.25 ± 0.87 (2SE) to -1.68 ± 0.59 (2SE) and from -4.84 ± 2.01 (2SE) to 0.07 ± 1.36 (2SE) for allanite (Fig. 9; Supplementary Table C1). The error bars for analyses of allanite are systematically larger than for monazite due to lower Nd concentration in allanite. Overall, the data acquired on monazite and allanite within a given sample are all within uncertainties of the WR isotopic compositions (Fig. 9). The studied samples show WR εNd_{55Ma} ranging between -3.18 ± 0.24 (2SE) and -1.74 ± 0.25 (2SE). Low uncertainties obtained on WR allow for the distinction of two different groups: one composed of B39, B23, KB1a and B26 with an average εNd_{55Ma}

of – 3.07 ± 0.16 (2SD) and the other consisting of B40, B21 and KB3 with an average εNd_{55Ma} of – 2.08 ± 0.59 (2SD). WR $^{147}Sm/^{144}Nd$ ratios show low dispersion, ranging from 0.1008 to 0.1249 (Table 2).

Discussion

Trace element variations in accessory minerals along the metamorphic gradient

The geological context of the CMC allows for a detailed examination of the chemical behaviour of accessory phases across a restricted metamorphic gradient of approximatively 150 °C, from greenschist to upper amphibolite facies under water-saturated melting conditions and minor muscovite breakdown. This study focuses particularly on apatite and monazite, which are systematically present in all samples along this gradient. This provides insights into the factors influencing their chemical signatures such as bulk rock, co-crystallisation of other minerals, evolving *P–T* up to partial melting. This study focuses on water-saturated melting reaction at 650–700 °C. It is worth noting that melting reaction can also greatly affect accessory minerals chemical signatures. For instance, it has been recently demonstrated by Liu et al. (2023) that apatite chemistry is particularly sensitive to the type of melting reactions (e.g. water-saturated melting, muscovite breakdown or amphibole breakdown).

Bulk influence on apatite, monazite and titanite chemistry

The influence of the sedimentary protolith (greywacke vs. pelite) on the chemistry of monazite and apatite is shown in Fig. 6. Monazite and apatite compositions for the metagreywacke samples (B21 and KB3) systematically differ from those of the metapelitic samples at the same metamorphic grade. They typically display higher HREE-Y contents (Fig. 6a, b) and lower Dy/Yb ratios (Fig. 6c, d). This trend can be attributed to the absence of garnet in these samples, which normally incorporates significant quantities of HREE-Y (e.g. Bea et al. 1994; Bea and Montero 1999; Foster et al. 2000; Rubatto et al. 2006), and the redistribution of these elements into apatite and monazite. Apatite from these two samples exhibits zoning patterns typical of dissolution-reprecipitation processes that are associated with an important spread in their trace element concentrations (REE, U, Th, etc.; Figs. 4b, c, f and 6a, c). Such textures are absent in apatite from metapelites. Apatite in sample B21 shows strong zoning with up to three different chemical zones in CL (Z1-Z2-Z3; Fig. 7a). Zones Z1 (core) and Z3 (rim) have higher concentrations of HREE-Y-Th compared to Z2 (Figs. 4f and 7b). These textures, only visible in the greywackes samples, may be the result of apatite partial dissolution during anatexis process, which is expected to be less efficient in greywackes than in pelites (e.g. Johnson et al. 2021). Another possibility would be that these textures formed by interactions with a late subsolidus fluid. However, as B21 does not exhibit any petrographic features indicating a late fluid circulation, we favour the first hypothesis.

Our observations show that titanite is present in the metagreywackes but appears very rarely in the metapelitic samples (only in KB1a; Table 1). Previous authors (Frost et al. 2001; Pereira et al. 2023) have suggested that Ca/Al and Ti/Ca whole-rock ratios favour titanite stability over ilmenite. The titanite stability over ilmenite can be explained by a higher $(Ca/Al)_{WR}$ and a lower $(Ti/Ca)_{WR}$ ratios of the samples ($Ca/Al > 0.25$, $Ti/Ca < 0.2$; Fig. 10a), while the other metapelitic samples have lower $(Ca/Al)_{WR}$ ranging between 0.10 and 0.25. The Y vs. Dy/Yb diagram has recently emerged as a tool to differentiate titanite crystallisation in garnet-bearing vs. garnet-free rocks (Scibiorski et al. 2019). In our study, all three samples plot within the garnet-absent field (Fig. 10b), which is consistent with the paragenesis of the two garnet-free metagreywackes but not

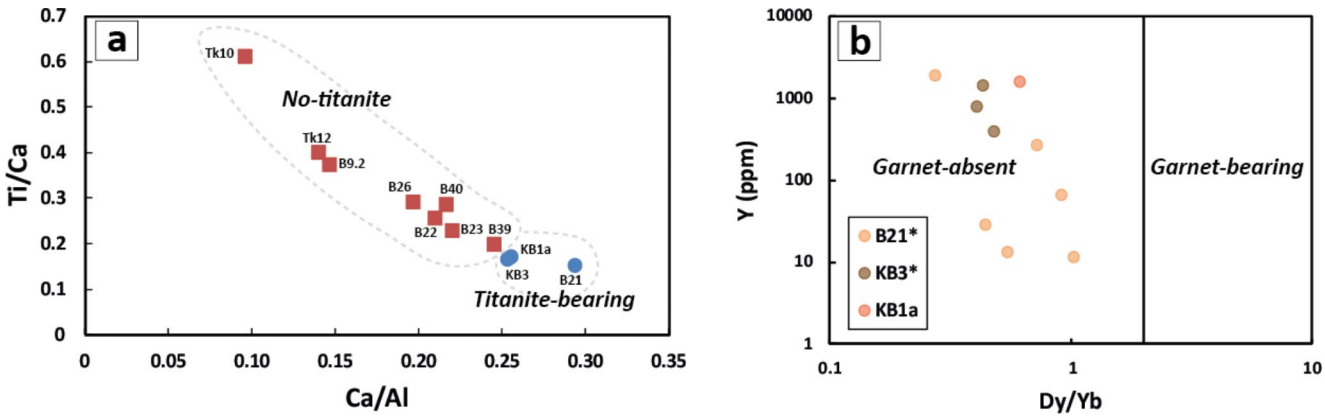

Fig. 10 **a** Ti/Ca vs. Ca/Al diagram with reported WR compositions of the CMC samples. **b** Y vs. Dy/Yb diagram for titanite from KB1a, KB3 and B21 samples (from Scibiorski et al. 2019). * = metagreywacke samples

with the metapelitic one which contains garnet. In this case, the very low modal proportion of garnet (~0.3%; Supplementary Table A2) in the metapelitic sample KB1a, could explain this apparent mismatch. Thus, these observations demonstrate the strong impact of the protolith chemistry and mineralogy on titanite stability and chemistry.

The two metagreywacke samples, B21 and KB3, are characterised by the presence of large allanite coexisting with monazite (Fig. 2e, f). This contrasts with the metapelites, which only contain small allanite crystals typically found in biotite cleavages, formed lately during greenschist facies retrogression. The sample B21 does not exhibit any retrogressed textures associated with allanite, suggesting that these minerals formed at peak metamorphism. Here, the absence of garnet, linked to the bulk composition, might be responsible for the development of these large allanite crystals, as proposed by Gasser (2010). In sample KB3, textures indicate the destabilisation of monazite into allanite (Supplementary Fig. A1a), with some large allanite crystals found in domains enriched in oxide, chlorite and late-stage titanite (Figs. 2f and 3i, j). These allanite grains are late-stage products of retrogression and exhumation under greenschist facies conditions (Gasser et al. 2012b). Given the absence of garnet in KB3, and the overlap of the REE-Y patterns of allanite grains of both samples (Fig. 8b), the possibility that some allanite grains could have been formed during peak metamorphism cannot be excluded, although textures indicate that most of the grains have formed during retrogression.

Apatite and monazite chemical sensitivity to increasing T and partial melting

This study has shown that bulk chemistry plays a major role in the chemical signatures of apatite and monazite. To understand the chemical sensitivity of these phases to increasing metamorphic grade and discard the bulk-rock influence, this section focuses on samples with similar pelitic protoliths. From the phyllite ($T<550$ °C) to the schist zones (550–630 °C), an intra-sample homogenisation of apatite chemical composition (REE and Sr contents) can be observed (Figs. 4 and 5a). This homogenisation is interpreted as the effect of prograde metamorphism on detrital apatite grains, already reported in previous studies (Hammerli et al. 2014, 2016), and will not be further discussed here. In the schist and migmatite dataset, two main trends in apatite and monazite can be observed with increasing grade: (i) an increase in the HREE-Y content and (ii) a decrease in Eu/Eu* (Figs. 6a, b and 11).

HREE-Y as a proxy of temperature and partial melting

The increase of HREE-Y content in apatite and monazite along the CMC metamorphic gradient can be influenced by several parameters such as (i) an increase of whole-rock trace element contents, (ii) variations in the modal proportions of HREE-Y phases (e.g. garnet, zircon, xenotime) and (iii) the release of HREE-Y elements due to the dissolution of other HREE-Y rich phases. The last two parameters are promoted by changes in *P-T* conditions. An increase of WR trace element contents is ruled out in the case of the CMC, as Y content along the gradient is nearly constant (Y = 25.5–30 ppm for the schist zone and 11.8–26.9 ppm for the migmatitic gneiss zone; Supplementary Table A1). Similarly, there are no clear trends in the evolving modal proportions of REE-Y rich phases from pelitic schists to migmatitic gneisses (Supplementary Table A2). For example, first-order estimates of garnet modal proportion calculated from thin section imaging range between 0.8 and 8.6% in the schist zone and between 0.3 and 8.2% in the migmatitic gneiss zone.

The partial dissolution of other HREE-Y bearing phases such as xenotime or zircon during anatexis, or the breakdown of garnet during retrograde metamorphism, can release HREE-Y into the system (e.g. Yakymchuk et al. 2017), which could then be redistributed in monazite and apatite. Garnet is the major mineral carrying HREE-Y. In high-grade metamorphic terranes, several studies showed that HREE-Y can be released during retrograde metamorphism by the breakdown of garnet, allowing the new growth of Y-rich rims in monazite (e.g. Foster et al. 2004; Kohn et al. 2005; Rubatto et al. 2013; Wang et al. 2017). In our samples, some garnet grains in both schists and migmatitic gneisses show limited resorbed rims (< 40 µm) with higher Mn and lower Mg contents (Bruand et al. 2014). Y-mapping and trace elements in garnet analysed in one sample by Gasser et al. (2012b) revealed no HREE-Y core-to-rim variations. These features are typical of thermal relaxation by diffusion and/or retrograde net transfer reaction between garnet and biotite during cooling (e.g. Kohn et al. 2001). In the CMC, monazite U-Pb ages (between 53.4 ± 1.1 Ma and 51.0 ± 1.1 Ma; Gasser et al. 2012b) are coeval with the dated anatectic rim of zircon (between 54.0 ± 0.7 Ma and 51.3 ± 0.7 Ma; Gasser et al. 2012a), showing that monazite crystallised at or close to peak metamorphism. This is further confirmed by the monazite-xenotime thermometer (Chowdhury and Trail 2024) applied to B23 migmatitic gneiss giving temperatures between 605 and 684 °C, which are consistent with *T* estimates from other thermometric methods previously obtained on this sample or other gneisses (e.g. Bt-Grt, average-*PT* on THERMOCALC; Table 1). Apatite also crystallised close to peak metamorphism as indicated by its occurrence in leucosomes (Supplementary Fig. A1g) and its chemical behavior similar to monazite proving that they both co-crystallised. If garnet contributed to the release of HREE-Y to the system, these observations highlight that it

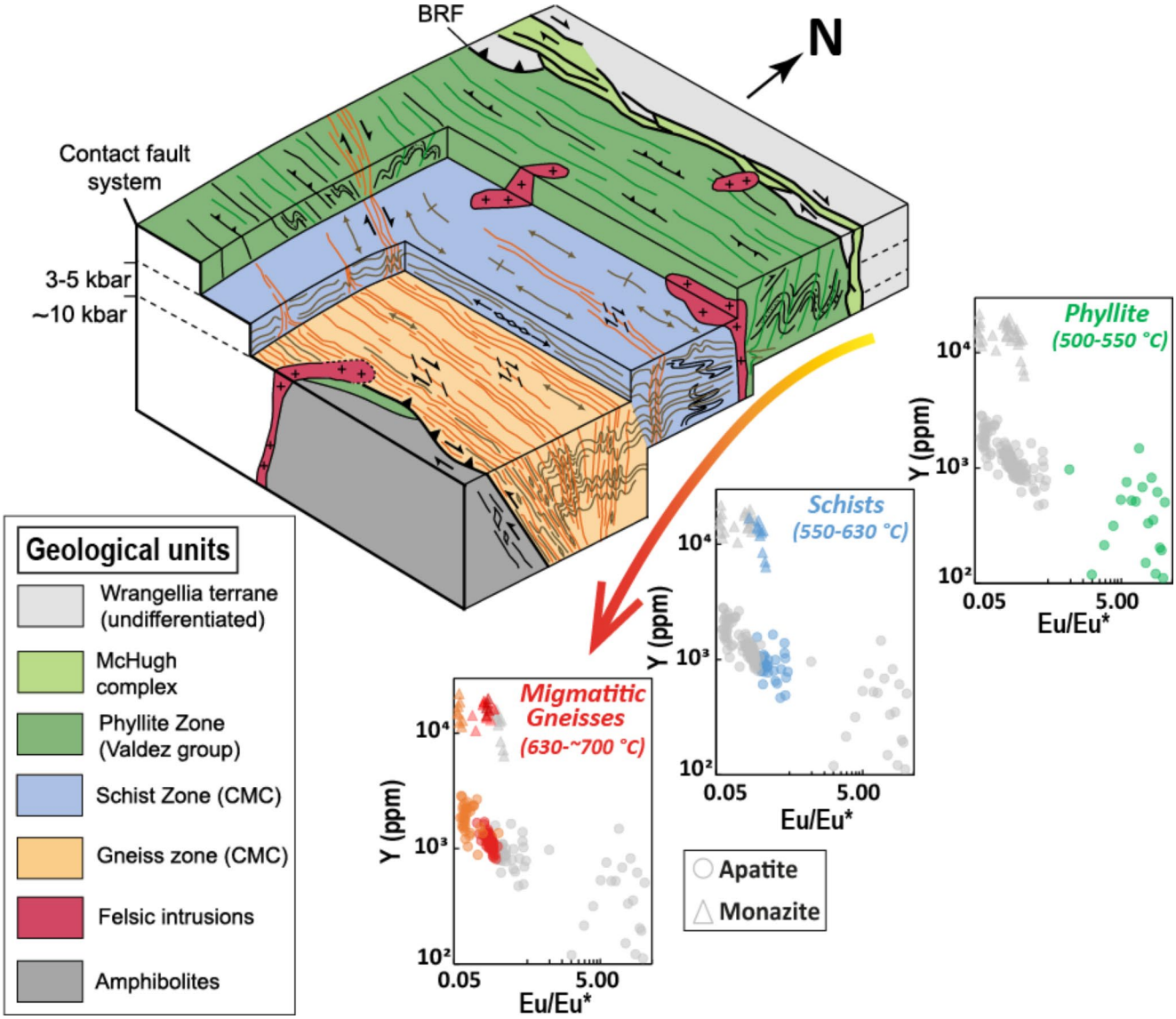

Fig. 11 3D schematic diagram of the northwestern part of the CMC (modified from Gasser et al. 2011) with the chemical behaviour of apatite and monazite in a Y (ppm) vs. Eu/Eu* diagram from the greenschist facies rocks (phyllite) to the upper amphibolite facies rocks (migmatitic gneisses). Samples colours are the same as in Fig. 6. Temperatures are from Bruand et al. (2014). Structural features are from Gasser et al. (2011)

has to be during the early cooling in order to be incorporated by apatite and monazite at the time of their crystallisation close to peak metamorphism.

Xenotime is often very small (< 20 µm) and quite rare in thin section, albeit systematically present in our samples. Xenotime is expected to be partly dissolved during anatexis in water-saturated conditions in a pelitic system (e.g. Spear and Pyle 2010; Yakymchuk et al. 2017; Johnson et al. 2021). However, no clear decrease in the modal proportion of xenotime is visible between the schist and the migmatitic gneiss zones at the thin section scale (Supplementary Table A2). Interestingly, the presence of xenotime at the boundaries of quartz or feldspar grains in the leucosomes of some migmatitic gneisses shows that some of them recrystallised from the anatectic melt (Fig. 2e; Supplementary Fig. A1f). This involvement in the partial melting process highlights their potential role in the release of HREE-Y into the system during anatexis.

Zircon have been the subject of a detailed study by Gasser et al. (2012a) on separated grains. In the studied samples, zircon grains from migmatitic gneisses show dissolution textures with igneous detrital cores overgrown by a thin anatectic rim (5–30 µm in width; Fig. 3p, q) that formed at or close to peak metamorphism, crystallising from anatectic melts contemporaneously with plagioclase and monazite (Gasser et al. 2012a). These dissolution textures indicate that some

HREE-Y were mobilised during anatexis. Although some of them recrystallised at the rim of the zircon, some HREE-Y might have been redistributed into monazite and apatite, explaining their enriched HREE-Y patterns. The contribution of zircon must however be minor compared to that of xenotime which is at least 100 times more concentrated in HREE-Y.

In summary, we consider the dissolution of xenotime during anatexis coupled to the potential resorption of garnet during early cooling as possible mechanisms releasing HREE-Y, which are further incorporated by apatite and monazite during their crystallisation close to peak metamorphism. Several studies on natural samples (Heinrich et al. 1997; Pyle et al. 2001), experiments (Gratz and Heinrich 1997) and modelling (Spear and Pyle 2010) have shown that Y incorporation in monazite increases with temperature in xenotime-bearing metapelitic samples under sub-solidus and supra-solidus conditions, leading to the development of the monazite-xenotime thermometer recently re-evaluated by Chowdhury and Trail (2024). Similarly, based on a limited dataset, Yang and Rivers (2002) suggested that Y in apatite when co-existing with xenotime might be sensitive to temperature increase. In this contribution, we confirm that apatite chemistry is sensitive to temperature changes in pelitic systems buffered by the presence of xenotime and that HREE-Y content in apatite has the potential to be used as a geothermometer.

Eu/Eu as a partial melting proxy*

Our dataset shows a decrease in Eu/Eu* in apatite and monazite along the metamorphic gradient. Eu anomaly variations in accessory phases (zircon, monazite, apatite) under anatectic conditions have been documented in numerous studies (e.g. Bea and Montero 1999; Rubatto 2002; Rubatto et al. 2006, 2013; Holder et al. 2015), and have traditionally been attributed to the behaviour of K-feldspar or plagioclase, which are known to incorporate a significant amount of Eu (e.g. Bea and Montero 1999). In our samples, plagioclase is a very abundant phase (> 30% vol.). Its co-crystallisation from the melt could have generated a strong negative anomaly in apatite and monazite. K-feldspar is absent or very rare in these samples, ruling out a potential effect of this phase. More recently, oxygen fugacity or melt extraction have been inferred through modelling as other causes for observed changes in the Eu anomaly of accessory minerals (Holder et al. 2020). While oxygen fugacity is not constrained in the CMC, some of the migmatitic gneisses have likely undergone melt extraction as testified by some melanocratic layers in the migmatites or the presence of low-volume granitic plutons intruding the CMC, coeval with peak metamorphism and migmatisation (Gasser 2010). Thus, a minor effect of these last processes (especially melt extraction) on measured Eu anomaly cannot be ruled out.

Nd isotopic composition of accessory minerals along the metamorphic gradient

The Nd isotopic compositions of our samples and their Nd-bearing accessory minerals are very similar, with an average εNd_{55Ma} of -2.63 ± 1.47 (2SD) for monazite, -2.53 ± 2.18 (2SD) for allanite and associated ranges of WR εNd_{55Ma} between -3.18 ± 0.24 (2SE) and -1.74 ± 0.25 (2SE) along the metamorphic gradient at $T > 550$ °C (Fig. 9). These data confirm results obtained on metatexite-diatexite-granite WR (Ferreira et al. 2020), on garnet-monazite-WR (Wang et al. 2020), and on various accessory phases (Hammerli et al. 2014), showing a homogeneity of the Nd isotopic composition during high-grade metamorphism and partial melting. In their study, Hammerli et al. (2014) described a prograde pelite-greywacke metamorphic sequence comparable to the CMC, but with a wider range of temperatures from 350 to 400 °C to 650–700 °C. For example, at 350–400 °C, apatite exhibits a wide range of εNd values spanning almost 15 epsilon units above and below the WR value. This wide scatter of data in apatite grains is interpreted as reflecting detrital signatures. They showed that the Sm–Nd system in apatite and monazite is homogenised with the WR at ~ 500–550 °C, while allanite and titanite show homogeneity at lower temperatures (from ~ 350–400 °C, see review in Hammerli and Kemp 2021). For the CMC case study, WR and accessory minerals share similar Nd isotopes signature implying either that homogenisation of the Sm–Nd system took place at least from the schist zone (> 550 °C) or that the protolith of the schists and migmatites derived from a single, isotopically homogeneous source, without initial Nd isotope variations before metamorphism. Strong trace element variations measured in apatite from the lower grade phyllite (Figs. 4 and 5a) could be indicative of a wide variety of detrital sources, with potentially variable Nd isotopic compositions. Nevertheless, the small grain size and low Nd concentrations of apatite grains in the phyllite prevented in-situ Sm–Nd analyses to confirm this hypothesis.

Other studies focusing on WR data on leucosome-mesosome or granite/restite pairs have suggested Sm–Nd isotopic disequilibrium during partial melting (e.g. Ayres and Harris 1997; Zeng et al. 2005a, b; Gaeta et al. 2018; Wolf et al. 2019; Yang et al. 2022), which raised the question of the reliability of the Sm–Nd system as a source tracer (Hammerli and Kemp 2021). These potential disequilibria require specific conditions such as an isotopically heterogeneous source, relatively fast melting and crystallisation (+ extraction) of anatectic melts, preventing re-equilibrium with the source (Ayres and Harris 1997; Wolf et al. 2019; Wang et al. 2023). Our in-situ analyses on minerals align with the statement of Hammerli and Kemp (2021) assertion that Sm–Nd isotopic disequilibria in accessory phases are not expected

during partial melting because Sm–Nd is homogenised at high temperature (> 550 °C). Local disequilibria, which we did not observe in our samples, have been reported in some cases due to "shielding effects" (i.e. accessory phases enclosed within minerals such as garnet, impeding isotopic homogenisation; Spandler et al. 2018), and in open systems due to injections/contamination of external melts from isotopically different sources (Hammerli and Kemp 2021).

The data obtained on KB3 allanite, largely formed from the circulation of late fluids during retrogression into the greenschist facies, allow investigations on the capacity of a late fluid to create isotopic disequilibrium within the rock. Wang et al. (2023) demonstrated, through a multi-isotope approach ($\delta^{18}O$, $\delta^{26}Mg$, $^{87}Sr/^{86}Sr$), that isotopic disequilibria could appear during anatexis in fluid-flux melting conditions associated with the influx of external fluids coming from the dehydration of surrounding rocks. External fluids can therefore be associated with isotopic disequilibria within the host rock, particularly if they come from surrounding rocks of different nature and isotopic composition. In our case, KB3 allanite shows no significant differences in Nd isotopic composition with the WR analysed and the phases formed during HT metamorphism and partial melting. This suggests that the late fluid that circulated in these rocks, allowing allanite crystallisation, had a similar Nd isotopic signature to the CMC rocks, advocating for a homogeneous isotopic signature of the CMC and surrounding rocks.

Interestingly, the WR Nd isotopic data, associated with smaller uncertainties, show the presence of two significantly different groups, one towards $\varepsilon Nd_{55\ Ma}$ of – 3.07 and the other towards $\varepsilon Nd_{55\ Ma}$ of – 2.08. This small difference is not seen in minerals because of the larger analytical uncertainties obtained by LA-MC-ICP-MS. Small differences in εNd are however very commonly observed in whole-rock measurements in sedimentary systems (Vervoort et al. 2011). Measured Nd isotopic ratios are also consistent with data measured in sediments off the coast of Alaska with similar ages ($\varepsilon Nd_{45\ Ma} = -2.1 \pm 0.1$, $\varepsilon Nd_{53\ Ma} = -2.8 \pm 0.1$; Vervoort et al. 2011). WR $^{147}Sm/^{144}Nd$ ratios show low dispersion (Table 2), which tend to confirm an overall isotopic homogeneity throughout the CMC.

Conclusions

We measured trace element concentrations and Nd isotopic compositions of apatite, monazite, allanite and titanite in metapelites and metagreywackes along a metamorphic gradient from greenschist facies to upper amphibolite facies, reaching anatexis in water-saturated conditions at ~650–700 °C. Our data reveal a strong bulk composition effect in the observed REE patterns of apatite, monazite and titanite in the migmatitic gneisses. Specifically, apatite and monazite from garnet-free metagreywackes have systematically lower $(Dy/Yb)_N$ than those from metapelitic samples. We demonstrate the potential of monazite and apatite in metapelitic samples to finely track temperature increase (over a range of ~150 °C) and anatexis based on their trace element signatures. From schists to migmatitic gneisses, the two phases show notably : (i) an increase in HREE-Y, linked to their crystallisation close to peak metamorphism following xenotime dissolution and potential garnet resorption during early cooling and (ii) a decrease in Eu/Eu*, likely related to the crystallisation of plagioclase after partial melting. We found no significant difference in εNd between monazite, allanite and WR, regardless of the rock type analysed. This suggests (i) an overall homogeneity of the Nd isotopic composition above 550 °C and up to crustal anatexis conditions and (ii) an isotopic equilibrium between mineral and whole-rock, indicating that Sm–Nd isotopic disequilibria are highly unlikely during partial melting in this case study.

Supplementary Information The online version contains supplementary material available at https://doi.org/10.1007/s00410-024-02185-2.

Acknowledgements We are grateful to M. Gannoun for his help provided with the LA-MC-ICPMS analyses as well as to J.-L. Devidal and J. Langlade for assistance with EPMA. We also thank E. Voyer and N. Gayet for technical assistance on the MEB in Clermont-Ferrand and Brest and Chantal Bosq for the help provided with Nd chemical separations. Lastly, we thank R. Doucelance for his stimulating discussion on Nd isotopes. This work was supported by the French National Research Agency (grant ANR-21-CE49-0001-01, AMNESIA, PI EB). I. Pereira acknowledges funding from the Portuguese National Science Foundation I.P. (Portugal) for a fellowship contract under the Individual Call to Scientific Employment Stimulus (2021.01616.CEECIND/CP1656/CT0006; https://doi.org/10.54499/2021.01616.CEECIND/CP1656/CT0006) and grants UIDB/00073/2020 and UIDP/00073/2020 awarded to Centro de Geociências (Universidade de Coimbra – Portugal). We thank R. Salerno and an anonymous reviewer for their constructive comments and suggestions that have greatly improved the quality of the manuscript.

Author contributions Théo Biget: Investigation, Formal analysis, Visualization, Writing – original draft, Writing – review & editing. Emilie Bruand: Conceptualization, Supervision, Investigation, Project administration, Funding acquisition, Writing – original draft, Writing – review & editing. Ines Pereira: Supervision, Investigation, Writing – review & editing. Maud Boyet: Formal analysis, Writing – review & editing. Deta Gasser: Writing – review & editing. Kurt Stüwe: Writing – review & editing, Resources. Antonio Langone: Writing – review & editing.

Declarations

Conflict of interest The authors declare that they have no known competing financial interests or personal relationships that could have appeared to influence the work reported in this paper.

References

Ayres M, Harris N (1997) REE fractionation and Nd-isotope disequilibrium during crustal anatexis: constraints from himalayan leucogranites. Chem Geol 139:249–269. https://doi.org/10.1016/S0009-2541(97)00038-7

Bea F, Pereira MD, Stroh A (1994) Mineral/leucosome trace-element partitioning in a peraluminous migmatite (a laser ablation-ICP-MS study). Chem Geol 117(1–4):291–312. https://doi.org/10.1016/0009-2541(94)90133-3

Bea F, Montero P (1999) Behavior of accessory phases and redistribution of Zr, REE, Th Y and U during metamorphism and partial melting of metapelites in the lower crust: an example from the Kinzigite Formation of Ivrea-Verbano, NW Italy. Geochim Cosmochim Acta 63:1133–1153. https://doi.org/10.1016/S0016-7037(98)00292-0

Bingen B, Demaiffe D, Hertogen J (1996) Redistribution of rare earth elements, thorium, and uranium over accessory minerals in the course of amphibolite to granulite facies metamorphism: the role of apatite and monazite in orthogneisses from southwestern Norway. Geochim Cosmochim Acta 60(8):1341–1354. https://doi.org/10.1016/0016-7037(96)00006-3

Bouvier A, Vervoort JD, Patchett PJ (2008) The Lu–Hf and Sm–Nd isotopic composition of CHUR: constraints from unequilibrated chondrites and implications for the bulk composition of terrestrial planets. Earth Planet Sci Lett 273:48–57. https://doi.org/10.1016/j.epsl.2008.06.010

Bradley D, Kusky T, Miller R, Dumoulin J, Nelson SW, Karl S (2003) Geologic signature of early tertiary ridge subduction in Alaska. Geol Soc Am Special Paper 371:19–50. https://doi.org/10.1130/0-8137-2371-X.19

Brown M, Rushmer T (2006) Evolution and differentiation of the Continental Crust. Cambridge University Press, Cambridge, UK. https://doi.org/10.1017/S0016756806273059

Bruand E (2010) A petrological study of the Chugach Metamorphic Complex in southern Alaska. PhD thesis, Department Of Earth Sciences, University of Graz, Graz, Austria, 204 pp

Bruand E, Gasser D, Stüwe K (2014) Metamorphic P–T conditions across the Chugach metamorphic complex (Alaska)—a record of focussed exhumation during transpression. Lithos 190–191:292–312. https://doi.org/10.1016/j.lithos.2013.12.007

Bruand E, Storey C, Fowler M, Dhuime B, Doucelance R (2023) Mineral-whole rock isotope fidelity? A comparative study of Hf-Nd-O from high Ba-Sr granitoids. Chem Geol 624:121425. https://doi.org/10.1016/j.chemgeo.2023.121425

Chowdhury W, Trail D (2024) A new experimental monazite-xenotime thermometer: application to metamorphic environments. Chem Geol 648:121939. https://doi.org/10.1016/j.chemgeo.2024.121939

Deng XD, Li JW, Wen G (2014) Dating iron skarn mineralization using hydrothermal allanite-(La) U-th-pb isotopes by laser ablation ICP-MS. Chem Geol 382:95–110. https://doi.org/10.1016/j.chemgeo.2014.05.023

Doucelance R, Bruand E, Matte S, Bosq C, Auclair D, Gannoun A-M (2020) In-situ determination of nd isotope ratios in apatite by LA-MC-ICPMS: challenges and limitations. Chem Geol 119740. https://doi.org/10.1016/j.chemgeo.2020.119740

Dusel-Bacon C (1994) Metamorphic history of Alaska. In: Plafker, George, Berg, H.C. The Geology of Alaska: Boulder, Colorado. Geological Society of America, G-1. The Geology of North America, pp 495–533

Engi M (2017) Petrochronology based on REE-minerals: Monazite, allanite, xenotime, apatite. Rev Mineral Geochem 83:365–418. https://doi.org/10.2138/rmg.2017.83.12

Ferreira A, Mata J, Bento dos Santos T, Pereira I (2020) The role of melting on the geochemical evolution and isotopic variability of an anatectic complex in the Iberian variscides. Lithos 378–379:105769. https://doi.org/10.1016/j.lithos.2020.105769

Fisher CM, McFarlane CRM, Hanchar JM, Schmitz MD, Sylvester PJ, Lam R, Longerich HP (2011) Sm–Nd isotope systematics by laser ablation-multicollector inductively coupled plasma mass spectrometry: methods and potential natural and synthetic reference materials. Chem Geol 284:1–20. https://doi.org/10.1016/j.chemgeo.2011.01.012

Fisher CM, Hanchar JM, Miller CF, Phillips S, Vervoort JD, Whitehouse MJ (2017) Combining nd isotopes in monazite and hf isotopes in zircon to understand complex open-system processes in granitic magmas. Geology 45:267–270. https://doi.org/10.1130/G38458.1

Fisher CM, Bauer AM, Luo Y, Sarkar C, Hanchar JM, Vervoort JD, Tapster SR, Horstwood M, Pearson DG (2020a) Laser ablation split-stream analysis of the Sm–Nd and U-Pb isotope compositions of monazite, titanite, and apatite – improvements, potential reference materials, and application to the Archean Saglek Block gneisses. Chem Geol 119493. https://doi.org/10.1016/j.chemgeo.2020.119493

Fisher CM, Bauer AM, Vervoort JD (2020b) Disturbances in the sm – nd isotope system of the Acasta Gneiss complex — implications for the nd isotope record of the early earth. Earth Planet Sci Lett 530:115900. https://doi.org/10.1016/j.epsl.2019.115900

Forshaw JB, Pattison DRM (2023) Major-element geochemistry of pelites. Geology 51:39–43. https://doi.org/10.1130/G50542.1

Foster G, Kinny P, Vance D, Prince C, Harris N (2000) The significance of monazite u-th-pb age data in metamor-phic assemblages; a combined study of monazite and garnet chronometry. Earth Planet Sci Lett 181:327–340. https://doi.org/10.1016/S0012-821X(00)00212-0

Foster G, Parrish RR, Horstwood MSA, Chenery S, Pyle J, Gibson HD (2004) The generation of prograde P-T–t points and paths; a textural, compositional, and chronological study of metamorphic monazite. Earth Planet Sci Lett 228(1–2):125–142. https://doi.org/10.1016/j.epsl.2004.09.024

Frost BR, Chamberlain KR, Schumacher JC (2001) Sphene (titanite): phase relations and role as a geochronometer. Chem Geol 172:131–148. https://doi.org/10.1016/S0009-2541(00

Gaeta M, Giuliani A, Rocco TD, Tecchiato V, Perinelli C, Kamenetsky VS (2018) Isotopic disequilibrium in migmatitic hornfels of the Gennargentu igneous complex (Sardinia, Italy) records the formation of low 87Sr/86Sr melts from a Mica-rich source. J Petrol 59:1309–1328. https://doi.org/10.1093/petrology/egy062

Garçon M, Boyet M, Carlson RW, Horan MF, Auclair D, Mock TD (2018) Factors influencing the precision and accuracy of nd isotope measurements by thermal ionization mass spectrometry. Chem Geol 476:493–514. https://doi.org/10.1016/j.chemgeo.2017.12.003

Gasser D (2010) Evolution of the Chugach Metamorphic Complex of southern Alaska in space and time. PhD thesis, Department Of Earth Sciences, University of Graz, Graz, Austria, 315 pp

Gasser D, Bruand E, Stüwe K, Foster D, Schuster R, Fügenschuh B, Pavlis T (2011) Formation of a metamorphic complex along an obliquely convergent margin: structural and thermochronological evolution of the Chugach Metamorphic Complex, southern Alaska. Tectonics 30. https://doi.org/10.1029/2010TC002776

Gasser D, Rubatto D, Bruand E, Stüwe K (2012a) Large-scale, short-lived metamorphism, deformation, and magmatism in the Chugach metamorphic complex, southern Alaska: a SHRIMP U–Pb study of zircons. Geol Soc Am Bull 124:886–905. https://doi.org/10.1130/B30507.1

Gasser D, Bruand E, Rubatto D, Stüwe K (2012b) The behaviour of monazite from greenschist facies phyllites to anatectic gneisses: an example from the Chugach Metamorphic Complex, southern Alaska. Lithos 134–135:108–122. https://doi.org/10.1016/j.lithos.2011.12.003

Gieré R, Sorensen SS (2004) Allanite and other REE-rich epidote-group minerals. Rev Mineral Geochem 56:431–493. https://doi.org/10.2138/gsrmg.56.1.431

Gonçalves GO, Lana C, Scholz R, Buick IS, Gerdes A, Kamo SL, Corfu F, Marinho MM, Chaves AO, Valeriano C, Nalini HA Jr (2016) An assessment of monazite from the Itambé pegmatite district for use as U–Pb isotope reference material for microanalysis and implications for the origin of the Moacyr monazite. Chem Geol 424:30–50. https://doi.org/10.1016/j.chemgeo.2015.12.019

Gratz R, Heinrich W (1997) Monazite–xenotime thermobarometry: experimental calibration of the miscibility gap in the binary system CePO4–YPO4. Am Mineral 82:772–780. https://doi.org/10.2138/am-1997-7-816

Gregory CJ, McFarlane CRM, Hermann J, Rubatto D (2009) Tracing the evolution of calc-alkaline magmas: In-situ Sm–Nd isotope studies of accessory minerals in the Bergell Igneous complex, Italy. Chem Geol 260:73–86. https://doi.org/10.1016/j.chemgeo.2008.12.003

Gregory CJ, Rubatto D, Hermann J, Berger A, Engi M (2012) Allanite behaviour during incipient melting in the southern Central Alps. Geochim Cosmochim Acta 84:433–458. https://doi.org/10.1016/j.gca.2012.01.020

Griffin WL, Powell WJ, Pearson NJ, O'Reilly SY (2008) GLITTER: data reduction software for laser ablation ICP-MS. In: Sylvester P (ed) Laser ablation–ICP–MS in the Earth Sciences. Mineralogical Association of Canada Short Course Series, vol 40, pp 204–207

Hammerli J, Kemp AIS (2021) Combined hf and nd isotope microanalysis of co-existing zircon and REE-rich accessory minerals: high resolution insights into crustal processes. Chem Geol 581:120393. https://doi.org/10.1016/j. chemgeo.2021.120393

Hammerli J, Kemp AIS, Spandler C (2014) Neodymium isotope equilibration during crustal metamorphism revealed by in situ microanalysis of REE-rich accessory minerals. Earth Planet Sci Lett 392:133–142. https://doi.org/10.1016/j. epsl.2014.02.018

Hammerli J, Spandler C, Oliver NHS (2016) Element redistribution and mobility during upper crustal metamorphism of metasedimentary rocks: an example from the eastern Mount Lofty Ranges, South Australia. Contrib Mineral Petrol 171:36. https://doi.org/10.1007/s00410-016-1239-7

Hammerli J, Kemp AIS, Whitehouse MJ (2019) In situ trace element and Sm–Nd isotope analysis of accessory minerals in an Eoarchean tonalitic gneiss from Greenland: implications for Hf and Nd isotope decoupling in Earth's ancient rocks. Chem Geol 524:394–405. https://doi.org/10.1016/j.chemgeo.2019.06.025

Hansen EC, Harlov DE (2007) Whole-rock, phosphate, and Silicate Compositional trends across an Amphibolite- to Granulite-facies transition, Tamil Nadu, India. J Petrol 48:1641–1680. https://doi.org/10.1093/petrology/egm031

Hayden LA, Watson EB, Wark DA (2008) A thermobarometer for sphene (titanite). Contrib Mineral Petrol 155:529–540. https://doi.org/10.1007/s00410-007-0256-y

Heinrich W, Rehs G, Franz G (1997) Monazite–xenotime miscibility gap thermometry. I. An empirical calibration. J Metamorph Geol 15:3–16. https://doi.org/10.1111/j.1525-1314.1997.t01-1-00052.x

Henrichs IA, Chew DM, Sullivan GJO, Mark C, Mckenna C, Guyett P (2019) Trace element (Mn-Sr-Y-Th-REE) and U-Pb isotope systematics of metapelitic apatite during progressive greenschist- to amphibolite-facies barrovian metamorphism. Geochem Geophys Geosyst 20(8):4103–4129. https://doi.org/10.1029/2019GC008359

Holder RM, Hacker BR, Kylander-Clark ARC, Cottle JM (2015) Monazite trace element and isotopic signatures of (ultra) high-pressure metamorphism: examples from the western Gneiss Region, Norway. Chem Geol 409:99–111. https://doi.org/10.1029/2020GC009052

Holder RM, Yakymchuk C, Viete DR (2020) Accessory mineral eu anomalies in suprasolidus rocks: beyond feldspar. Geochem Geophys Geosyst 21. https://doi.org/10.1029/2020GC009052.e2020GC009052

Hudson T, Plafker G (1982) Paleogene metamorphism of an accretionary flysch terrane, eastern Gulf of Alaska. Geol Soc Am Bull 93:1280–1290. https://doi.org/10.1130/0016-7606(1982)932.0.CO;2

Ickert R (2013) Algorithms for estimating uncertainties in initial radiogenic isotope ratios and model ages. Chem Geol 340:131–188. https://doi.org/10.1016/j.chemgeo.2013.01.001

Iizuka T, Eggins SM, McCulloch MT, Kinsley LPJ, Mortimer GE (2011) Precise and accurate determination of 147Sm/144Nd and 143Nd/144Nd in monazite using laser ablation-MC-ICPMS. Chem Geol 282:45–57. https://doi.org/10.1016/j.chemgeo.2011.01.008

Jochum KP, Willbold M, Raczek I, Stoll B, Herwig K (2005) Chemical characterisation of the USGS reference glasses GSA-1G,GSC-1G, GSD-1G, GSE-1G, BCR-2G, BHVO-2G and BIR-1G using EPMA, ID-TIMS, ID-ICP-MS and LA-ICP-MS. Geostand Geoanal Res 29(3):285–302. https://doi.org/10.1111/j.1751-908X.2005.tb00901.x

Johnson T, Yakymchuk C, Brown M (2021) Crustal melting and suprasolidus phase equilibria: from first principles to the state-of-the-art. Earth Sci Rev 221:103778. https://doi.org/10.1016/j.earscirev.2021.103778

Kohn MJ, Kelly NM (2018) Petrology and geochronology of metamorphic zircon. Microstructural Geochronology: Planet Records down atom Scale 35–61. https://doi.org/10.1002/9781119227250.ch2

Kohn MJ, Catlos EJ, Ryerson FJ, Harrison TM (2001) Pressure–temperature–time path discontinuity in the Maine Central thrust zone, central Nepal. Geology 29:571–574. https://doi.org/10.1130/0091-7613(2001)0292.0.CO;2

Kohn MJ, Wieland MS, Parkinson CD, Upreti BN (2005) Five generations of monazite in Langtang gneisses: implications for chronology of the Himalayan metamorphic core. J Metamorph Geol 23(5):399–406. https://doi.org/10.1111/j.1525-1314.2005.00584.x

Kunz BE, Regis D, Engi M (2018) Zircon ages in granulite facies rocks: decoupling from geochemistry above 850°C? Contrib Mineral Petrol 173:1–21. https://doi.org/10.1007/s00410-018-1454-5

Liu S, Zhang G, Li H (2023) Fingerprinting crustal anatexis with apatite trace element, halogen, and Sr isotope data. Geochim Cosmochim Acta 351:14–31. https://doi.org/10.1016/j.gca.2023.04.021

Lugmair GW, Marti K (1978) Lunar initial 143Nd/144Nd differential evolution of lunar crust and mantle. Earth Planet Sci Lett 39:349–357. https://doi.org/10.1016/0012-821X(78)90021-3

Marks MA, Wenzel T, Whitehouse MJ, Loose M, Zack T, Barth M, Worgard L, Krasz V, Nelson Eby G, Stosnach H, Markl G (2012) The volatile inventory (F, Cl, Br, S, C) of magmatic apatite: an integrated analytical approach. Chem Geol 291:241–255. https://doi.org/10.1016/j.chemgeo.2011.10.026

McDonough WF, Sun S (1995) The composition of the Earth. Chem Geol 120:223–253. https://doi.org/10.1016/0009-2541(94)00140-4

O'Sullivan G, Chew D, Kenny G, Henrichs I, Mulligan D (2020) The trace element composition of apatite and its application to detrital provenance studies. Earth Sci Rev 201:103044. https://doi.org/10.1016/j.earscirev.2019.103044

Palma G, Barra F, Reich M, Valencia V, Simon AC, Vervoort J, Leisen M, Romero R (2019) Halogens, trace element concentrations, and Sr-Nd isotopes in apatite from iron oxide-apatite (IOA) deposits in the Chilean iron belt: evidence for magmatic and hydrothermal stages of mineralization. Geochim Cosmochim Acta 246:515–540. https://doi.org/10.1016/j.gca.2018.12.019

Pereira I, Bruand E, Nicollet C, Koga KT, Brovarone AV (2023) Ti-Bearing minerals: from the Ocean Floor to Subduction and back. J Petrol 64:1–26. https://doi.org/10.1093/petrology/egad041

Pin C, Briot D, Bassin CP, Poitrasson F (1994) Concomitant separation of strontium and samarium-neodymium for isotopic analysis in silicate samples, based on specific extraction chromatography. Anal Chim Acta 298(2):209–217. https://doi.org/10.1016/0003-2670(94)00274-6

Pyle JM, Spear FS, Rudnick RL, McDonough WF (2001) Monazite–xenotime–garnet equilibrium in metapelites and a new monazite–garnet thermometer. J Petrol 42:2083–2107. https://doi.org/10.1093/petrology/42.11.2083

Pyle JM, Spear FS, Wark DA (2002) Electron microprobe analysis of REE in apatite, monazite and xenotime: protocols and pitfalls. Rev Mineral Geochem 48(1):337–362. https://doi.org/10.2138/rmg.2002.48.8

Rubatto D (2002) Zircon trace element geochemistry: partitioning with garnet and the link between U–Pb ages and metamorphism. Chem Geol 184:123–138. https://doi.org/10.1016/S0009-2541(01)00355-2

Rubatto D, Hermann J, Buick IS (2006) Temperature and bulk composition control on the growth of monazite and zircon during low-pressure anatexis (Mount Stafford, central Australia). J Petrol 47(10):1973–1996. https://doi.org/10.1093/petrology/egl033

Rubatto D, Chakraborty S, Dasgupta S (2013) Timescales of crustal melting in the higher himalayan crystallines (Sikkim, Eastern Himalaya) inferred from trace element constrained monazite and zircon chronology. Contr Mineral Petrol 165:349–372. https://doi.org/10.1007/s00410-012-0812-y

Sawyer EW, Press NRCR (2008) Special Publication 9. 371. https://doi.org/10.1139/9780660197876

Sawyer EW, Cesare B, Brown M (2011) When the continental crust melts. Elements 7:229–234. https://doi.org/10.2113/gselements.7.4.229

Scharman M, Pavlis TL, Ruppert N (2012) Crustal stabilization through the process of ridge subduction: examples from the Chugach Metamorphic Complex, southern Alaska. Earth Planet Sci Lett 329–330:22–132. https://doi.org/10.1016/j.epsl.2012.02.020

Schneider CA, Rasband WS, Eliceiri KW (2012) NIH Image to ImageJ: 25 years of image analysis. Nat Methods 9:671–675. https://doi.org/10.1038/nmeth.2089

Scibiorski E, Kirkland CL, Kemp AIS, Tohver E, Evans NJ (2019) Trace elements in titanite: a potential tool to constrain polygenetic growth processes and timing. Chem Geol 509:1–19. https://doi.org/10.1016/j.chemgeo.2019.01.006

Shaw DM (1956) Geochemistry of pelitic rocks. PartIII: major elements and general geochemistry. Geol Soc Am Bull 67:919–934. https://doi.org/10.1130/0016-7606(1956)67[919:GOPRPI]2.0.CO;2

Shrestha S, Larson KP, Duesterhoeft E, Soret M, Cottle JM (2019) Thermodynamic modelling of phosphate minerals and its implications for the development of P-T-t histories: a case study in garnet – monazite bearing metapelites. Lithos 334–335:141–160. https://doi.org/10.1016/j.lithos.2019.03.021

Sisson VB, Hollister LS, Onstott TC (1989) Petrologic and age constraints on the origin of a low-pressure/high-temperature metamorphic complex, Southern Alaska. J Geophys Res 94:4392–4410. https://doi.org/10.1029/JB094iB04p04392

Sisson VB, Poole AR, Harris NR, Cooper Burner H, Pavlis TL, Copeland P, Donelick RA, McLelland WC (2003) Geochemical and geochronologic constraints for genesis of a tonalite-trondhjemite suite and associated mafic intrusive rocks in the eastern Chugach Mountains, Alaska: a record of ridge-transform subduction. In: Sisson VB, Roeske SM, Pavlis TL (eds) Geology of a transpressional orogen developed during ridge-trench interaction along the North Pacific margin: Boulder, Colorado, Geological Society of America Special Paper, vol 371, pp 293–326

Skrzypek E, Kato T, Kawakami T, Sakata S, Hattori K, Hirata T, Ikeda T (2018) Monazite behaviour and timescale of metamorphic processes along a low-pressure/high-temperature field gradient (Ryoke belt, SW Japan). J Petrol 59(6):1109–1144. https://doi.org/10.1093/petrology/egy056

Spandler C, Hammerli J, Pirard C (2018) Neodymium isotope disequilibria in subducted sediments, and potential consequences for subduction-zone recycling. Geology 46:815–818. https://doi.org/10.1130/G45147.1

Spear FS, Pyle JM (2010) Theoretical modeling of monazite growth in a low-Ca metapelite. Chem Geol 273:111–119. https://doi.org/10.1016/j.chemgeo.2010.02.016

Sun J-F, Yang J-H, Zhang J-H, Yang Y-H, Zhu Y-S (2021) Apatite geochemical and Sr-Nd isotopic insights into granitoid petrogenesis. Chem Geol 566:120104. https://doi.org/10.1016/j.chemgeo.2021.120104

Vervoort JD, Plank T, Prytulak J (2011) The Hf-Nd isotopic composition of marine sediments. Geochim Cosmochim Acta 75:5903–5926. https://doi.org/10.1016/j.gca.2011.07.046

Volante S, Blereau E, Guitreau M, Tedeschi M, van Schijndel V, Cutts K (2023) Current applications using key mineral phases in igneous and metamorphic geology: perspectives for the future. In: van Schijndel V, Cutts K, Pereira I, Guitreau M, Volante S, Tedeschi M (Eds.) 2024 Minor Minerals, Major Implications: Using Key Mineral Phases to Unravel the Formation and Evolution of Earth's Crust. Geological Society, London, Special Publications 537: 57–121. https://doi.org/10.1144/jgs2013-115

Wang J-M, Wu F-Y, Rubatto D, Liu S-R, Zhang J-J, Liu X-C, Yang L (2017) Monazite behaviour during isothermal decompression in pelitic granulites: a case study from Dinggye, Tibetan Himalaya. Contrib Mineral Petrol 172:81. https://doi.org/10.1007/s00410-017-1400-y

Wang D, Fisher CM, Vervoort JD, Cao H (2020) Nd isotope re-equilibration during high temperature metamorphism across an orogenic belt: evidence from monazite and garnet. Chem Geol 119751. https://doi.org/10.1016/j.chemgeo.2020.119751

Wang D, Shirey SB, Carlson RW, Fisher CM, Kemp AI, Bickford ME (2022) Comparative Sm–Nd isotope behavior of accessory minerals: reconstructing the Sm–Nd isotope evolution of early Archean rocks. Geochim Cosmochim Acta 318:190–212. https://doi.org/10.1016/j.gca.2021.11.031

Wang Y, Wu H, He Y, Ke S, Li S, Wang S-J (2023) Isotope disequilibrium caused by the influx of fluids during crustal anatexis. Chem Geol 634:121567. https://doi.org/10.1016/j.chemgeo.2023.121567

Wasserburg G, Jacobsen S, DePaolo D, McCulloch M, Wen T (1981) Precise determination of Sm/Nd ratios, Sm and Nd isotopic abundances in standard solutions. Geochim Cosmochim Acta 45:2311–2323. https://doi.org/10.1016/0016-7037(81)90085-5

Whitney DL, Evans BW (2010) Abbreviations for names of rock-forming minerals. Am Mineral 95:185–187. https://doi.org/10.2138/am.2010.3371

Williams MA, Kelsey DE, Rubatto D (2022) Thorium zoning in monazite: a case study from the Ivrea–Verbano Zone, NW Italy. J Metamorph Geol 40(6):1–22. https://doi.org/10.1111/jmg.12656

Wolf M, Romer RL, Glodny J (2019) Isotope disequilibrium during partial melting of metasedimentary rocks. Geochim Cosmochim Acta 257:163–183. https://doi.org/10.1016/j.gca.2019.05.008

Yakymchuk C, Brown M (2014) Behaviour of zircon and monazite during crustal melting. J Geol Soc 171(4):465–479. https://doi.org/10.1144/jgs2013-115

Yakymchuk C, Clark C, White RW (2017) Phase relations, reaction sequences and petrochronology. Rev Mineral Geochem 83:13–53. https://doi.org/10.2138/rmg.2017.83.2

Yang P, Rivers T (2002) The origin of Mn and Y Annuli in Garnet and the thermal dependence of P in garnet and Y in apatite in calc-pelite and pelite, Gagnon terrane, western Labrador. Geol Mat Res 4:1–35

Yang L, Wang J-M, Liu X-C, Khanal GP, Wu F-Y (2022) Sr-Nd-Hf Isotopic Disequilibrium during the partial melting of metasediments: insight from Himalayan Leucosome. Front Earth Sci 10:891960. https://doi.org/10.3389/feart.2022.891960

Zeng LS, Asimow PD, Saleeby JB (2005a) Coupling of anatectic reactions and dissolution of accessory phases and the Sr and nd isotope systematics of anatectic melts from a metasedimentary source. Geochim Cosmochim Acta 69:3671–3682. https://doi.org/10.1016/j.gca.2005.02.035

Zeng LS, Saleeby JB, Asimow PD (2005b) Nd isotope disequilibrium during crustal anatexis: a record from the Goat Ranch migmatite complex, southern Sierra Nevada batholith, California. Geology 33:53–56. https://doi.org/10.1130/G20831.1

Zhang W, Hu Z, Liu Y, Chen H, Gao S, Gaschnig RM (2012) Total rock dissolution using ammonium bifluoride (NH4HF2) in screw-top Teflon vials: a New Development in Open-Vessel digestion. Anal Chem 84:10686–10696. https://doi.org/10.1021/ac302327g